INTERNATIONAL ATOMIC ENERGY AGENCY
UNITED NATIONS EDUCATIONAL, SCIENTIFIC AND CULTURAL ORGANIZATION
INTERNATIONAL CENTRE FOR THEORETICAL PHYSICS
I.C.T.P., P.O. BOX 586, 34100 TRIESTE, ITALY, CABLE CENTRATOM TRIESTE

SMR/459 - 3

SPRING COLLEGE IN CONDENSED MATTER ON:
PHYSICS OF LOW-DIMENSIONAL SEMICONDUCTOR STRUCTURES

(23 APRIL - 15 JUNE 1990)

ELECTRONIC PROPERTIES IN SEMICONDUCTOR
HETEROSTRUCTURES

L.J. SHAM
Department of Physics
Univeristy of California, San Diego
La Jolla, California 92093-3019
U.S.A.

Electronic Properties in Semiconductor Heterostructures

L. J. Sham
Department of Physics
University of California, San Diego
La Jolla, California 92093-3019, USA

Contents

1. INTRODUCTION

Modern methods of epitaxial growth,[1] the Molecular Beam Epitaxy (MBE) and the Metallo-Organic Chemical Vapor Deposition (MOCVD), have provided the capability of fabricating a hugh variety of thin (5 - 100 Å) layers of different semiconductor compounds on a substrate, with interfaces of atomic precision. These semiconductor heterostructures generate a new set of physics as well as devices. These systems can be separated into two classes:

1. Heterojunctions and quantum wells: The former is composed of two compounds, denoted by A and B, with electrons (or holes) confined at the interface. The latter is a sandwich of the form ABA, where the central layer may or may not contain charge carriers depending on whether the system is doped or undoped. In both heterojunctions and quantum wells, the charge carriers are confined in two dimensions. The special features are high mobility, discrete levels in high normal magnetic fields and strong electron-electron interaction because of the enforced confinement. In these lectures, we shall examine the consequences of these characteristics.

2. Superlattices: A superlattice is composed of a periodic array of semiconductor compounds, e.g. of the form ABAB..., in thin layers. Tunneling between barriers is an important characteristic. By contrast, a multiple quantum well of similar composition, ABAB..., has wide barriers so that carriers are confined to separated wells. While some features of experimental observations can be explained by the simple Kronig-Penney model, for many important electronic properties in the superlattice the role of the interface is crucial. We shall study some of these issues here.

In section 2, the basic electron properties due to confinement in a simple quantum well model are presented. Justification of the square well model in terms of an extension of the effective mass theory is described in section 3. A particularly important concept, which determines the electronic behavior across an interface, is the band-edge offset, which is the change in the energy of the bulk conduction band minimum or the valence band maximum on crossing from one semi-infinite medium into another while the electronic behavior in each region is kept the same as the corresponding bulk semiconductor by some means. We examine the physics which determines the offset in order to understand the theories for calculating the offset as well as the empirical determination. In section 4, consideration of the relative positions of the valence and conduction band edges of the two constituent compounds leads to a variety of electronic behavior, which is conveniently classified into three types of quantum wells and superlattices.

Section 5 covers the electronic structure in superlattices, including both the Kronig-Penney model and the mixing of electrons from different valleys. Section 6 studies the effects of a large magnetic field. A magnetic field normal to the interface separates the subbands into discrete Landau levels, producing striking observable properties. A magnetic field parallel to the interface controls the crossing of the interfaces and, thus, provides an excellent means of studying tunneling through a barrier.

The lectures up to this point deal with the effect of the heterostructure on the electron, namely the one-electron properties. The rest of the lectures deal with many-body effects. The doped quantum well is a superb laboratory for studying many-body effects because of the ease with which the parameters of the system can be changed by applying an electric field, a magnetic field, or a stress. Section 7 examines the self-energy effect, which is particularly dramatic as a function of a normal magnetic field. Photo-luminescence is an important tool in the characterization of electronic states of the quantum wells and superlattices. Section 9 investigates in some detail the processes involving in photo-luminescence, including relaxation mechanisms by phonon scatterings and by shake-up of a Fermi sea. The synthesis of the one-electron subbands and the many body effects leads to understanding of a beautiful array of phenomena observed in luminescence experiments.

2. BASIC ELECTRONIC PROPERTIES IN QUANTUM WELLS

2.1. Typical Band Structure of Bulk Semiconductors

Many of the electronic properties in a quantum well can be extracted from the electrons and holes near the band edges in a bulk semiconductor, using a modified effective mass approximation.[2] For a typical direct-gap semiconductor, such as GaAs (Fig. 1), the conduction band edge wave function is s-like (Γ_1) and the valence band edge is p-like (Γ_{15}) with a three-fold degeneracy.[3] Taking into account the spin-orbit interaction, the s-like Γ_1 states become Γ_6, which are still a total angular momentum J=1/2 doublet. The p-like states are split into Γ_8, or J=3/2 states with a four-fold degeneracy, and Γ_7 states, or J=1/2 with a two-fold degeneracy. The spin-orbit splitting is generally large enough for the higher energy Γ_8 states to be considered separately in a qualitative consideration but not so large that in quantitative calculations Γ_7 can be neglected.

2.2. Electron Confinement

The basic principle is simple. In a quantum well of, say, $Al_xGa_{1-x}As/GaAs/Al_xGa_{1-x}As$, the conduction band edge energy of GaAs lies in the band gap of AlGaAs. Thus, a conduction electron in GaAs will not be able to escape deep into AlGaAs and is thus confined, and its energy level is quantized (Fig. 2). The conduction band edge of the two compounds form a square well potential from which the normal (z-axis) motion quantization can be calculated. The in-plane motion is free-electron like with the conduction band effective mass m^*. The effective mass equation for the envelope function is given by

$$\left[-\frac{\hbar^2}{2m^*}\left(\frac{\partial^2}{\partial x^2}+\frac{\partial^2}{\partial y^2}\right)-\frac{\hbar^2}{2m^*}\frac{\partial^2}{\partial z^2}+V(z)-E\right]\psi=0 \qquad (1)$$

The resulting discrete subbands as functions of the momentum parallel to the interface plane are shown in Fig. 3 with a constant density of states to each subband. More elaborate

boundary conditions across the interfaces[4] are not essential when the conduction band edges of the two semiconductors are close to each other but are necessary when the band offsets are comparable to the band gaps, such as in InAs/GaSb or InSb quantum wells.

The sandwich structure of undoped semiconductors contains no carriers and is called an undoped quantum well. If the outer layers of the quantum well (AlGaAs in our present example) are doped with donors (acceptors), electrons (holes) will be trapped in the GaAs well. A spacer layer of undoped AlGaAs between the doped barrier and the GaAs well further separates the carriers from the doping impurities and thus achieves very high mobility. This technique of introducing doping is called modulation doping.[5]

Because the dimension of a quantum well is between the microscopic ($\sim$ 1Å) and the macroscopic (1 μm) scale, a number of typical dimensions should be kept in mind. For a quantum well of thickness of 100Å, the typical wave-vector is about 10^{-2}/Å. For an electron density of 10^{11} cm^{-2}, the Fermi energy is of the order 10 meV for the effective mass m^* of 0.1 times the free electron mass. In a magnetic field of 1 Tesla, the cyclotron resonance is about 3×10^{11} Hz or 1 meV for the same effective mass.

2.3. Hole Subbands

A frequently used approximation for the valence bands is two sets of parabolic bands, one with a heavy effective mass m_{hh}, thus called the heavy holes, and one with a light mass, $m_{\ell h}$, called the light holes. (For GaAs, $m_{hh} \simeq 0.4$ and $m_{\ell h} \simeq 0.1$.) While this approximation is certainly simple in concept, it does not even reproduce significant qualitative features of the hole subbands in a quantum well. We shall avoid this approximation. I hope to convince you that the complex of degenerate valence subband is not that difficult to visualize and that out of it come some very nice physics.

To deduce the valence subbands in a heterostructure, we again start with the bulk band structure. Consider only the set of four bands degenerate at the top of the va

lence bands at Γ_8 (J=3/2). Represent the wave function of a state by four components, defined by the z-component of the angular momentum (normal to the interfaces), $m_J = 3/2, 1/2, -1/2, -3/2$. The k.p Hamiltonian was deduced by Luttinger[6] from symmetry considerations. For the quantum well, the motion parallel to the interface again has plane wave for all four components of the wave function with wave vector $\mathbf{k} = (k_x, k_y)$. The 4×4 Hamiltonian matrix has the form

$$H_v = \begin{bmatrix} P+Q & -S & R & 0 \\ -S^\dagger & P-Q & 0 & R \\ R^\dagger & 0 & P-Q & S \\ 0 & R^\dagger & S^\dagger & P+Q \end{bmatrix}, \tag{2}$$

where:

$$P \pm Q = -\frac{\hbar^2}{2m}(\gamma_1 \mp 2\gamma_2)\frac{\partial^2}{\partial z^2} + V(z) + \frac{\hbar^2}{2m}(\gamma_1 \pm \gamma_2)(k_x^2 + k_y^2)$$

$$R = -\tfrac{\hbar^2}{2m}\sqrt{3}\gamma k_-^2, \qquad \gamma = \tfrac{1}{2}(\gamma_2 + \gamma_3)$$

$$R_A = \tfrac{\hbar^2}{2m}\sqrt{3}\mu k_+^2, \qquad \mu = \tfrac{1}{2}(\gamma_3 - \gamma_2)$$

$$S = \sqrt{3}\tfrac{\hbar^2}{m}\gamma_3 k_- \cdot \tfrac{1}{i}\tfrac{\partial}{\partial z}, \quad k_\pm = k_x \pm i k_y.$$

The γ's are the Luttinger parameters for the valence band, m is the free electron mass. The diagonal terms $P \pm Q$ contain, in order, the z-components of the motion with the effective square well potential, the kinetic energy terms in the x-y plane. The expression for R is called the cylindrical approximation since it preserves the rotation symmetry about the z-axis for the Hamiltonian. For the full Luttinger expression, the anisotropic correction R_A must be added to the R terms.

The structure of the Luttinger Hamiltonian can be understood as follows. In the cylindrical approximation (neglecting the R_A terms), the form of the Hamiltonian, quadratic in k_x, k_y, $k_z = \frac{1}{i}\frac{\partial}{\partial z}$ conserves angular momentum about the z-axis. $k_\pm = k_x \pm i k_y$ are isomorphous to the angular momentum raising and lowering operators. k_z does not affect

the z-component of the angular momentum. For example,

$$< 3/2|H|1/2 > \;=\; -S \propto k_- k_z. \tag{3}$$

Since the spin m_J is raised from 1/2 to 3/2 (in units of $\hbar$), the orbital angular momentum must be lowered by unity and, hence, the factor k_-. Similarly,

$$< 3/2|H|-1/2 > \;\propto\; k_-^2, \tag{4}$$

(neglecting the R_A term in the cylindrical approximation), lowers the orbital angular momentum by 2 to compensate for the increase of the spin. $< 3/2|H|-3/2 >$ would require three factors of k_- and, therefore, vanishes in the quadratic approximation.

If the off-diagonal terms of the Luttinger Hamiltonian are neglected, we have a parabolic approximation for holes, but note the essential difference with the naive version described at the beginning of this section. The $m_J = \pm 3/2$ components are degenerate, having a parabolic energy dispersion having an effective mass in the z-direction as heavy:

$$m_{hz} \;=\; \frac{1}{\gamma_1 - 2\gamma_2}. \tag{5}$$

If one of the $m_J = \pm 3/2$ components of a state dominates, we might refer to the state as a heavy hole state. The effective mass components of the "heavy" hole parallel to the interface plane are light:

$$m_{h\|} \;=\; \frac{1}{\gamma_1 + \gamma_2}. \tag{6}$$

Similarly, the $m_J = \pm 1/2$ components yield the light holes with light mass along the z-axis

$$m_{lz} \;=\; \frac{1}{\gamma_1 + 2\gamma_2} \tag{7}$$

and moderately heavy mass parallel to the interface plane

$$m_{l\|} \;=\; \frac{1}{\gamma_1 - \gamma_2}. \tag{8}$$

For GaAs, the Luttinger parameters are $\gamma_1 = 6.85$, $\gamma_2 = 2.10$, and $\gamma_3 = 2.90$. The heavy hole masses are $m_{h_z} = 0.38$ and $m_{h\|} = 0.11$. The light hole masses are $m_{\ell_z} = 0.09$ and $m_{\ell\|} = 0.21$.

In a layer bounded by impenetrable walls, the Luttinger Hamiltonian can be solved analytically.[7] In the following, we shall concentrate on the AlGaAs/GaAs system, for which the boundary conditions of continuous wave function components and their gradients are quite adequate for bound hole states in GaAs.[8]

Since $\mathbf{k} = (k_x, k_y)$ remains a good quantum number, in the center of the two dimensional Brillouin zone, $k = 0$, the Hamiltonian becomes diagonal and the states are eigenstates of m_J ($\pm 3/2$ for heavy holes and $\pm 1/2$ for light holes). These states are used as the basis set in the mini k.p method to obtain all the subband states.[8] While this basis set may not be the best for computational purpose,[8-11] it can serve that purpose and, moreover, it serves as a useful way to visualize a general valence subband state as a mixture of m_J states due to k.p matrix elements. We shall demonstrate later how this method can be used to understand the optical transition between the conduction and valence subbands.

In the Luttinger Hamiltonian, if the parameters γ_2 and γ_3 are nearly equal, then the R_A term proportional to μ can be dropped. The energy subbands are isotropic in k, the wave-vector parallel to the interface plane. This is the approximation referred to above as the cylindrical approximation. The μ term, though small, can have an important effect in some cases. For example, in the heterojunction there is spin splitting of the top heavy-hole subband. One component has a nearly circular Fermi surface and the other is nearly square when the μ term is included.[6] On the other hand, where averages over k about the z-axis are involved, such as in the optical spectrum or in a Landau level, the cylindrical approximation is adequate.[12]

Figure 4, after Ref. 13, is a typical example of valence subbands in an undoped AlGaAs/GaAs/AlGaAs quantum well. Under the cylindrical approximation, the bands are

isotropic in k. At $k = 0$, the states are eigenstates of m_J (h for $\pm 3/2$ and ℓ for $\pm 1/2$). The subband index is given by integers starting with 1 in descending order of the energy. In the figure, only the top two heavy hole bands and the top light hole band are shown. The dot-dash lines are in the parabolic approximation in the sense of neglecting the off-diagonal terms (S and R) of the Luttinger Hamiltonian. Note that the heavy hole bands ($m_J = \pm 3/2$) have a lighter in-plane mass than the light hole bands ($m_J = \pm 1/2$). When the off-diagonal terms are included, the proximity of the second heavy-hole band pushes up the 1ℓ light hole band so that, for small k, the light hole band is actually electron-like.[9] Although the finite k states are mixtures of different m_J states, the subbands are unambiguously labeled h or ℓ because of their lineage at $k = 0$.

The $1h$ and 1ℓ subbands look as if they might cross in some systems and the $k.p$ terms split them apart again. Examination of the wave functions show that at k values larger than the uncrossing point, the $1h$ band is dominated by the $m_J = \pm 1/2$ components and vice versa.

3. INTERFACE EFFECTS ON ELECTRONS

The simple potential models described in the last section lead to electron subbands for the GaAs/AlGaAs systems which are well verified by experiments, some of which we shall discuss below. There remain systems which cannot be described by such simple effective potentials. Even for cases where the models work, one may ask why, knowing the fact that the effective mass approximation is usually derived for a potential additional to the crystal potential which is slowly varying. The square well potential due to the heterostructure contains abrupt jumps. In this section we describe a theory which extends the effective mass theory to abrupt ideal interfaces[2] and then give an account of the theoretical concept of band offset and its empirical determination.

3.1. Effective Mass Theory for Heterostructures

Consider the electron motion governed by a one-particle Schrödinger equation with the potential given by the crystal potential plus any contribution from charge distribution and due to the exchange-correlation effect *a la* the density functional theory.[14] The heterostructure is conceptually divided into bulk homogeneous semiconductor regions bounded by interface regions consisting of 1-3 atomic layers. (See Figure 5.)

In the bulk region, the electron potential has a large component due to the periodic lattice potential of the homogeneous semiconductor and a spatially gradually varying potential due to charge redistribution and external fields. The effect of the crystal potential is accounted for by expanding the electron wave function in this region in terms of Bloch waves of the periodic potential. For energies close to the band edge, the linear combination is approximated by an amplitude modulation of the Bloch waves near the band edge. The envelope function then is governed by an effective Schrödinger equation with the effective potential given by the slowly varying component only.

In connecting the wave function from one bulk region to another, the true wave function and its normal derivative must be continuous throught the interface region. It is then important to remember that the bulk region is finite and the Bloch waves in each region consist of evanescent as well as propagating waves. In the interior of the bulk regions, the envelope function is a modulation of the propagating Bloch waves. The evanescent waves contribute only at the interface.

The slowly varying component of the potential is unimportnt in the narrow interface region. In the language of the scattering theory, the propagating Bloch waves in one bulk region are scattered into different channels of Bloch waves in a neighboring region. The coefficients of the S-matrix may be used to determine the boundary conditions for the envelope function. In Ref. 2, examples of construction of the S-matrix are given for the

model of an interface being a geometric plane. The general concept applies to any model of the interface. The presence of the evanescent waves means that, *a priori*, there is no reason why the envelope wave function or its derivative need be continuous. Examples will be given in the following section.

3.2. Band Offsets

Consider a heterostructure of two dissimilar semi-infinite semiconductors. In the flat-band condition described in the foregoing subsection, an electron in one of the two bulk regions will be like in the corresponding bulk semiconductor. Let the difference in valence band edge energy between the two bulk regions be ΔE_v. The electron at the higher lying valence band edge is connected to the propagating Bloch waves in the other bulk region. The electron at the lower valence band edge has, in the other region, an evanescent wave. The two states can be simulated by the effective mass potential step, ΔE_v. This quantity, called the valence band offset, is clearly a fundamental input to the effective potential model for the heterostructure. If the band gap difference between the same pair of semiconductors is denoted by ΔE_g, the conduction band edge is given by

$$\Delta E_c = \Delta E_g - \Delta E_v. \tag{9}$$

The offset is often measured as a fraction of the band gap difference, e.g.

$$Q_v = \Delta E_v / \Delta E_g. \tag{10}$$

What contributes to the valence band offset? In a heterostructure, usually a superlattice,[15,16] the electronic charge density is determined self-consistently in the density functional theory.[14] The resulting self-consistent electrostatic potential has a constant cell average in each bulk region. The difference between the potential averages in the two bulk regions, $\Delta\phi$, is due to the dipole layer formed from re-arranging the bulk electron density in the interface region. In each bulk semiconductor, the valence band edge energy is then calculated relative to the

same potential cell average. Let the difference of the bulk valence band energy be ΔE_v^B. The valence band offset is the sum

$$\Delta E_v = \Delta E_v^B + \Delta\phi. \tag{11}$$

While the theoretical contributions to the band offset are now clear, a self-consistent local density approximation calculation of the superlattice requires large scale computation. What we need is a simple model which contains the essence of the contributions to the band offset. It is found[15,16] that the dipole term, $\Delta\phi$, is small compared with the bulk difference, ΔE_v^B. This agrees with the empirical findings of weak dependence on the orientation of the interface and of transitivity: the offset between A and B is the sum of the offsets between A and C and between C and B. Tersoff[17] gave a nice reasoning for the dipole term to be small. As stated above, the valence states in the range ΔE_v above the lower valence band edge penetrate into the interface region with decaying evanescent waves, which constitute one component of the interface dipole. Similarly, the decaying waves from the conduction band offset will also contribute to the dipole. This dipole layer then acts to lower the offsets in order to minimize the dipole moment and thus to lower the electrostatic energy.

Two similar models[15,16] are designed to neglect the small dipole term and to define the bulk potential zero in order to determine the bulk valence energy difference, ΔE_v^B. In each bulk region the energy zero is defined by a potential average. While the same averaging method must be used in both regions, the definition of the average is not unique. (1) Start with the superposition of neutral atomic spheres.[15] The potential outside each sphere goes to zero, which will be taken as the zero of energy for the bulk region. (2) The potential zero is defined by the periodic electron density of the bulk in each Wigner-Seitz cell.[16] There is also a model[18] which takes into account the orientation dependence of the dipole term.

There is a variety of empirical methods to determine the band offset:

1. Optical spectra of excitons. Because of confinement of the electron and hole in a quantum well the exciton lines dominate the optical spectra of transitions between the conduction and valence subbands, much more so than in three dimensional systems. By fitting the exciton lines from the square well model to experiment, the valence band offset quotient in GaAs/Al_xGa_{1-x}As was first[19] determined to be 15%. The value was accepted for almost a decade before Miller et al.[20] found from the optical transitions in a parabolic quantum well that the valence band offset quotient was much larger, about 50%. Careful fitting to additional forbidden exciton lines for the square quantum well[21] gave 43%. This shows the insensitivity of the exciton lines to the potential step size. Many other measurements have favored the larger valence band offset, with the commonly accepted value now being 34%, i.e 0.55 eV for GaAs/AlAs. For GaAs/Al_xGa_{1-x}, the offset is approximately linearly dependent on Al concentration, $0.55x$ eV.

2. X-point conduction valley. Later, we shall see how valley mixing allows optical transition between conduction subbands in the X-valleys and the Γ-valley valence subbands. From the pressure dependence of the photoluminescence lines[22] in GaAs/AlGaAsthe X-valley subbands can be identified. Since the X-valley potential minimum occurs in the AlGaAs layers and the valence potential maximum occurs in the GaAs layers, the valence band offset can be deduced from a knowledge of the transition energy plus the bulk indirect band gap and the small exciton correction because of the large X-valley effective mass.

3. Deep level impurity.[23,24] It was found that deep-lying transition metal impurity levels are fixed relative a common potential zero for a group of isovalent semiconductor compounds. The energies of the band edges relative to these deep levels may then be used to establish the band offsets.

4. X-ray photo-emission spectra.[25] One core level is selected from each semiconductor and the valence band edge is measured by XPS for each bulk. The difference in core energies is measured from the XPS for the heterojunction.

5. Internal photo-emission.[26] A structure of metal, a thin layer of GaAs and a layer of AlGaAs make up a Schottky barrier and a heterojunction. By measuring the onset of photo-current excited by light, the Schottky barrier height of GaAs and the height of AlGaAs are separately measured, from which the conduction band offset is measured.

6. Thermionic emission. In a sandwich of p-GaAs/AlGaAs/GaAs, from the temperature dependence of the thermionic emission current, the activitation energy yields the valence band offset.[27]

7. Charge transfer in heterojunction.[28] A modulation p-doped AlGaAs with a spacer layer of AlGaAs facing the GaAs heterojunction leads to a hole layer on the GaAs side of the interface. A low temperature de Haas-Shubnikov measurement determines the hole density. A model calculation of the heterojunction electrostatic potential leads to the hole density depending on the valence band offset. Comparison with experimentally determined density then fixes the offset.

8. Capacitance-voltage measurements.[29] As an alternative to the above, the conduction band offset of an n-channel GaAs/AlGaAs junction is determined from the capacitance dependence on gate voltage.

9. Raman scattering. Light scattering determines the intersubband energies in the conduction valley.[30] Model potential reproduction of the conduction subband energy spacings then determines the conduction band offset.

4. TYPES OF SUPERLATTICES

Esaki et al.[31] have classified the superlattices according to the band edge alignment. In some cases, it becomes necessary to treat the conduction and valence bands in the same complex of multi-band effective mass equations. We shall examine new physics which arise out of the conduction-valence $k \cdot p$ interaction via simple models.

4.1. Classification According to Band Edge Alignment

Figure 6 shows three types of superlattices depending on the relative positions of the band edges of the two compounds which make up the superlattice. Type I is typical, with the band gap of one semiconductor entirely in the band gap of the other. GaAs/AlGaAs superlattice is a famous example. Type II shows overlapping valence band of one semiconductor with the conduction band of the other. InAs/GaSb is an example. Recently, Type II is also taken to mean the valence band edge higher in one semiconductor and the conduction band edge lower in the other, regardless whether the overlap exists or not.[32] Type III shows Γ_8 and Γ_6 inversion of one semiconductor relative to another.

4.2. Two-Band Model

In section 2, the effective mass equations for the conduction band and the valences bands are considered separately. The $k \cdot p$ mixing between the conduction and valence bands is neglected because of the large band gap. The band interaction is important in a number of cases: Type I with a narrow gap semiconductor, such as InSb or $Cd_xHg_{1-x}Te$, Type I with a large offset, such as the conduction band in a GaAl/AlAs superlattice, and Type II superlattices. In principle, we can straight-forwardly use the multiband EMA, including eight bands, two from the Γ_6 conduction bands, four from the top Γ_8 valence bands, and two from the Γ_7 split-off bands. We shall use the simple two band model, including the conduction and light-hole band, to illustrate the important physics of band interaction.

With the basis of a pair of Γ_6 and Γ_8 Bloch waves, the 2×2 effective Hamiltonian is given by

$$H = \begin{bmatrix} V + \Delta & k_z P \\ k_z P & V - \Delta \end{bmatrix}. \tag{12}$$

Both V and Δ depend on z along the superlattice growth direction. In each layer, V represents the energy at the center of the gap and 2Δ the bulk band gap. In the two-band model, because of completeness and symmetry, the basis functions and P are assumed to be the same for both semiconductors.

Figure 7 shows the real and imaginary wave-vectors at a given energy for the true wave function to be matched at the boundary. By considering the limit of vanishing evanescent waves[2] or by assuming the continuity of one component of the envelope function,[33] or by simply integrating the Hamiltonian across a sharp interface with step function changes in V and Δ, the boundary conditions are derived that two components of the envelope function are continuous. Note that it does not follow that the derivatives are continuous. In fact, such conditions will over determine the 2×2 effective mass equations which are differential equations of first order. The Bag model for quark confinement, using the Dirac equation, has the same boundary conditions.[34]

In the GaAs/AlAs superlattice, the lowest conduction electron subbands are sufficiently close to the bulk conduction band edge that the parabolic bulk band approximation used in the effective mass equation is valid. However, the conduction band edge of AlAs is 1.06 eV above that of GaAs. The parabolic approximation for the evanescent wave in the AlAs barrier region using the AlAs Γ edge effective mass is clearly inappropriate. The energy of the electron subband is deep in the gap of AlAs and is treated in the extension of the two-band model.[35] A four-band model, including the s-state for the bulk conduction band and 3 p-states for the bulk valence bands, is adopted for both the GaAs wells and AlAs

barriers. The Hamiltonian is now

$$H = \begin{bmatrix} V + \Delta & k_x P & k_y P & k_z P \\ k_x P & V - \Delta & 0 & 0 \\ k_y P & 0 & V - \Delta & 0 \\ k_z P & 0 & 0 & V - \Delta \end{bmatrix}. \tag{13}$$

In the 4×4 effective mass equations, three components of the envelope functions are solved in terms of the s-wave component, f_s. By substituting them into the first equation, the set of 4×4 equations is reduced to a single Schrödinger-like equation:

$$\frac{\hbar^2}{2l^2}\left[-\frac{d}{dz}\frac{1}{m(z,E)}\frac{d}{dz} + \frac{(k_x)^2 + k_y^2}{m(z,E)}\right] f_s + [V(z) + \Delta(z) - E] f_s = 0, \tag{14}$$

where

$$m(z,E) = \hbar^2(E - V + \Delta)/2P^2. \tag{15}$$

Integrating Eq. (14) across the interface and letting the thickness of the small interface region tend to zero, we find the boundary conditions of f_s to be continuous and

$$\frac{1}{m(z,E)}\frac{d}{dz} f_s \tag{16}$$

to be continuous. These are just extensions of the Ben Daniel-Duke[36] boundary condition to energy levels deep in the gap.

Later, we shall study a tunneling experiment in the GaAs/AlAs superlattice where the conduction electron energy E is close to the GaAs conduction band edge, i.e. $\epsilon = E - V_w - \Delta_w$ may be treated as a small energy parameter in comparison to the gaps and offsets. To the leading order in ϵ,

$$m(z,E) = \begin{cases} m_w^* & \text{in the well} \\ m_b = m_b^* - Q_c(m_b^* - m_w^*) & \text{in the barrier} \end{cases} \tag{17}$$

where

$$m_{b,w}^* = \hbar^2 \Delta_{b,w}/P^2 \tag{18}$$

are the bulk masses. Note that the renormalized mass is equal to the bulk effective mass in the well region but not in the barrier. Taking the bulk effective-mass in the well, $m_w^* = 0.067m_e$, we find, within the approximation of the same basis functions and P for the well and the barrier, the bulk effective mass in the barrier to be $m_b^* = 0.14m_e$ and the renormalized mass to be $m_b = 0.09m_e$, i.e., a 35% reduction. Direct energy gaps of 1.52 eV for GaAs and 3.13 eV for AlAs and a band offset of $Q_c = 0.66$ are used in the above estimates.[37]

4.3. Metal-Insulator Transition in Type II GaSb/InAs

For thin enough layers, the electrons confined in InAs have higher energies than the holes in GaSb (Fig. 8a).[2] As the layer thickness increases, the decrease in zero-point energies will mean that the two subbands will overlap, resulting in a metal-insulating transition.[31] Figure 8b shows that, within the margin of uncertainty of the band offset (indicated by the double lines), energies (solid lines) using the boundary conditions of Eq. (12) yield better transition thickness than the square well model (dashed lines) in comparison with experiment[38] (80Å for each layer).

4.4. Type III HgTe/CdTe

Schulman and McGill have suggested[39] that quantum well confinement will turn the zero gap HgTe into small gap semiconductors, useful as infrared detectors. Unusual interface states are found theoretically.[40,41] They can be understood by the simple inversion of the light hole bands of HgTe above the light-hole band at Γ_8 of CdTe. The cusp of the envelope function (Fig. 9) at the interface boundary satisfies the boundary condition $\partial f_2/\partial z/m*$ being continuous. [See Sec. 4.2.] The inplane energy dispersion has interesting features, including termination of a subband at a finite wave vector.[42]

5. ELECTRONS IN SHORT-PERIOD SUPERLATTICES

A superlattice A_NB_M with each period composed of N layers of semiconductor A and M layers of semiconductor B is said to be a short period superlattice if N and M are small integers, say less than 10. We shall use the example of A being GaAs and B being AlAs. In a bulk III-V semiconductor compound, there are generally three sets of local conduction band minima, at Γ, X, and L. In GaAs, the conduction minimum at Γ is the lowest; in AlAs, the X point minimum is the lowest. Thus, in a superlattice, the conduction subbands from these valleys can mix. These mixing effects are consequences of the superlattice beyond the effective mass potential. They have been extensively studied both experimentally and theoretically. For reviews and comprehensive references, see Refs. 43 and 44. Here, we shall study a small number of fundamental issues in valley mixing.

5.1. The Kronig-Penney Model

In the Kronig-Penney, the periodic square well potential following the band edge alignment provides a zeroth order approximation for the conduction subbands in the superlattice. Figure 10 shows the band edge alignment[45] along the growth axis of the superlattice of $(GaAs)_N(AlAs)_M$ for the valence band edge and for the three important conduction valleys at Γ, X and L. The valence subband holes tend to be confined in the GaAs regions. The bulk Γ conduction valley is lower in the GaAs regions than in the AlAs regions and, thus, tends to confine the conduction electrons to the GaAs regions. The X valleys of AlAs lie lower than those in GaAs and tend to confine the electrons in the AlAs regions.

Because of the anistropy of the effective mass tensor of AlAs at the X point, (001), the effective mass parallel to the crystal axis is given by $m_l = 1.1$, and normal to the axis by $m_t = 0.2$. The zero point energy in the X_z or (001) valley due to confinment along the growth axis (001) with the larger effective mass m_l is smaller than the zero point

energy in the X_x (100) and X_y (010) valleys with the smaller effective mass m_t. Thus, the Kronig-Penney predicts that the lowest X_z subband lies lower than the X_x or X_y subbands.

Since the effective mass in the Γ valley of GaAs is 0.067, much smaller than either of the effective masses of the X valleys in AlAs, the zero point energy in the Γ well in GaAs regions is larger than that in the X_z well. If the GaAs region is sufficiently thick, the lowest Γ subband lies below the X_z subband and the superlattice has a direct gap from the Γ valence subband to the Γ conduction subband. If the GaAs region is sufficiently thin so that the Γ subband lies above the X_z, then the gap is "pseudo-direct" in the sense that the gap is direct in the superlattice Brillioun zone but in the optical transition the electron is excited from the GaAs region to the AlAs region. The transition from direct to pseudo-direct gap can be effected by varying the relative layer thickness,[46] by applying an electric field along the growth axis,[47] and by hydrostatic pressure[48] or uniaxial stress.[49] The optical transition in the pseudo-direct case is distinguished by the characteristics of lower optical efficiency, slower photoluminescence decay rate,[46] distinctive dependence on the longitudinal electric field,[47] different temperature dependence of energy gaps from that of the bulk GaAs gap,[46] and the g-value from the optically detected magnetic resonance.[50]

If we assume the superlattice to be perfectly lattice-matched, the lattice translational symmetry parallel to the interface plane, i.e. normal to (001) direction, is unchanged and the wave vector along the interface plane is still a good quantum number. Then the interfaces can scatter the Bloch waves from the Γ valley into the X_z valleys and vice versa. When the Γ and X_z subbands are close in energy, the mixing due to the interface is important and does not appear in the Kronig-Penney model. In the superlattice, X_x and X_y have equivalent wave vectors in the interface plane and can also have mixing by the interface.

5.2. Symmetry Properties of Superlattices

Unlike the Kronig-Penney model where the symmetry properties are trivial, the superlattice symmetry properties are important in considering the valley-mixing effects whether $\Gamma - X_z$ or $X_x - X_y$. In this section we collect a few important symmetry properties for an idealized superlattice with a period along the z-axis of N layers of an AB compound and M layers of an AD compound,[45] all atoms being on the sites of a zinc blende lattice with lattice constant a. The symmetry properties are unchanged if the spacings between the planes deviate from a. The coordinate axes are chosen as usual along the principal symmetry directions (100), etc.

The Bravais lattice of the zinc blende is fcc. Viewed along the z-axis, alternate planes of atoms of the same element do not lie on top of each other. The lattice vector covering one period of the superlattice points along the growth direction if $N+M$ is even and points along $(0,1,N+M)$ if $N+M$ is odd. Therefore, the Bravais lattices are different in the two cases. When $N+M$ is even, the Bravais lattice is simple tetragonal, with the basis vectors:

$$(1,1,0)a/2,\ \ (-1,1,0)a/2,\ \ (0,0,1)(N+M)a/2, \tag{19}$$

where a is the bulk lattice constant. When $N+M$ is odd, the Bravais lattice is body-centered tetragonal, with the basis vectors:

$$(1,1,0)a/2,\ \ (-1,1,0)a/2,\ \ (0,1,N+M)a/2. \tag{20}$$

The corresponding Brillouin zones are shown in Figs. 1(b) and 1(c). Different parts of the three dimensional fcc Brillouin zone are folded into a superlattice Brillouin zone as shown in Fig. 11.

Because of the inequivalence of the B and D planes, of the point group operations in T_d ($\bar{4}3m$), only those which do not change the z coordinates, i.e. C_{2z} (two-fold rotation about

the z-axis) and σ_v and $\sigma_{v'}$ (reflections in the $x = \pm y$ planes), and those which involve two fold rotations about the x and y axis (C_{2x}, C_{2y}), and the four-fold (improper) rotations about the z-axis *cum* reflection about the xy plane (S_{4z}, S_{4z}^3) survive as the point group operations leaving the superlattice invariant. These form the D_{2d} ($\bar{4}2m$) point group.[51] The space group is symmorphic and is D_{2d}^5 ($P\bar{4}m2$) when $N + M$ is even and D_{2d}^9 ($I\bar{4}m2$) when $N + M$ is odd.

Of particular interest are the subbands along the k_z direction through the bulk conduction valleys at Γ, X, and L, i.e. with wave vectors $(0, 0, fc^*)$, $(a^*, 0, fc^*)$, and $(a^*/2, a^*/2, fc^*)$ where

$$0 \leq f \leq 1, \quad a^* = 2\pi/a, \quad c^* = 2\pi/a(N + M). \tag{21}$$

Referring to Fig. 11, we put a bar over the symbol for a symmetry point in a superlattice Brillouin zone to distinguish it from the point in the bulk zone. The point groups associated with the various symmetry points for the superlattices along these three segments are given in Table I. The consequences of the difference in symmetry along $(a^*, 0, q)$ between the states labeled in $\overline{X}, \overline{T}, \overline{W}, \overline{Y}$ for odd $N + M$ and $\overline{M}, \overline{V}, \overline{A}$ for even $N + M$ will be shown later.

The space group operations can be divided into those not changing the z coordinate (denoted by E) and those changing z to -z (denoted by J). An A plane between a B and a D plane may be regarded as an interface plane between an AB region and an AD region. For an operation of J, the origin is at an atom equidistant from two nearest interface planes of A atoms. For definiteness, the origin will be chosen to be the mid-point in an AD region. Thus, it is at an A atom if M is even and at a D atom if M is odd. The representations in the bulk will be referred to the origin at an A atom. If we number along the z-axis the layers (each layer consisting of an A plane and a B or D plane), an even-numbered layer and an odd-numbered layer are staggered relative to each other whereas two layers, both even or odd numbered, lie directly on top of each other. When M is even, an operation of

J brings an even- (odd-) numbered A plane to another even- (odd-) numbered A plane and an even-numbered B or D plane to an odd-numbered B or D plane of the same species. When M is odd, the roles of the A and B or D planes are reversed. Thus, when a point group contains elements of J, the symmetry properties of the states are different for even and odd M, in addition to the difference due to $N + M$ being even or odd. The effects of this difference will become apparent later.

At a number of symmetry points, such as $\overline{\Gamma}$ and $\overline{A}$, we are interested in states with irreducible representations of unity under operations in E and ± 1 under J, which will be referred to, respectively, as even and odd parity states.

5.3. Computation Methods for Superlattice Electronic Structure

We refer to Ref. 44 for a recent review of the theory. There are two complementary approaches to the calculation of the electronic structure of a superlattice. The first-principles approach has the advantage of generating a self-consistent potential, taking into account the interface effect, and is useful for a small number of layers, for $N + M$ up to about 14. We shall concentrate here on the other approach, the empirical approach, which is based on the knowledge of the bulk band structures of the constituent compounds which make up the superlattice. Thus, a band structure method is adopted with the input parameters of the method "reverse-engineered" from the band structures of the constituent compounds in bulk form. The bulk parameters are applied to the interior layers of the corresponding compound. For the interface region, either averages of the bulk parameters for both compounds are taken or the atoms are assigned to either bulk region. In one study,[45] interface parameters are varied to study the effect on the superlattice subbands.

The tight binding method offers one framework for a superlattice subband calculation with empirical input.[52] The tight-binding interaction parameters involving two atomic

sites in the same material are chosen to reproduce the bulk bands and the band edge offset. The parameters involving two sites across the interface are taken to be averages of the bulk values. An appropriate choice of which bulk band features to fit is important for the accuracy of the subbands of the superlattice. For example, complete neglect of the next-nearest-neighbor interaction leads to an infinite transverse effective mass in the X-valleys of the bulk bands, with the consequence that the subbands from the X-valleys along the growth axis always lie above those from the inplane valleys, contrary to both experiment and the expectation from the effective mass approximation. Inclusion of the second-nearest-neighbor parameters[45] remove this difficulty. A partial study of the variation of the subband energies as functions of the interface parameters shows a weak dependence, justifying the use of the bulk average. The states studied do not, however, have large amplitudes in the interface regions.

The strength of the tight-binding method is in its chemical approach, since the bond parameters are local functions of the bulk semiconductor. The short-range interaction is particularly suited for the study of interface disorder, an important area for understanding horizontal and vertical transport, where much remains to be done. At present, the method suffers from lack of information on the physics of the interface, namely the cause of the band edge offset and the deviation of the tight-binding parameters in the interface region from the bulk values. This weakness is, however, in practice rather than in principle, unlike the EMA. The tight-binding framework would be very useful if the knowledge of the interface could be used to give the tight-binding parameters in the interface region. The possible avenues of using experimental results and of using results of first-principles band calculations in superlattices to fix the tight-binding parameters in the interface region should be explored.

The empirical pseudo-potential method gives another framework for the superlattice electron structure calculation.[53] The pseudopotential for each atom in the superlattice

is determined from the constituent of the bulk semiconductor. It is then assumed to be unchanged even in the interface region. A further simplification in calculation is possible if the atomic positions in the superlattice are taken to be in the ideal bulk lattice of one of the constituents. The zeroth order pseudopotential is taken either to be the average of the two compounds or that of one compound, and it produces a set of bulk bands. The difference between the superlattice potential and the zeroth order potential is treated as the superlattice potential which provides the deviation from the folding of the bulk bands from the zeroth order potential into the small superlattice Brillioun zone. This provides a very attractive way of tracking from zone folding the origin of the subbands.

The advantage over the EMA, which the pseudopotential method shares with the tight-binding method, is the avoidance of the wave function matching over a fictitious interface plane. The pseudopotential method is easier to use than the tight-binding method in fitting the bulk bands over a range of several electron volts but is more difficult to use in fitting finer features such as the effective tensors at a band edge or the spin-orbit splitting of the valence band edge. While the pseudopotential method shares with all empirical methods the inaccuracy of the interface atoms, it may be easiest to change the pseudopotentials of the interface atoms using the charge density distribution from a self-consistent computation of an interface.

5.4. Valley Mixing Between Γ and X

In Fig. 12 we plot the calculated[45] conduction subband energies at $\bar{\Gamma}$ as functions of N for the N/N superlattice. By comparing with the EMA results using the square wells, as shown in Fig. 10, and by examining the wave functions which are dominant in the GaAs or AlAs region, we identify the levels as from the Γ or X_z valley, denoted by $n\Gamma$ and nX with $n = 0, 1, \ldots$. Note that, because the Γ valley effective mass is small, the Γ levels are more widely spaced and increase in energy more rapidly than the X levels as N decreases. The

parity is defined in Sec. 5.2. The even (odd) parity states have irreducible representation $\overline{\Gamma}_1$ ($\overline{\Gamma}_3$), following the number system of Koster.[51] In the tight-binding representation, the coefficients of the S orbitals have the same parity as the state, and those of the P_z orbitals have the opposite parity. Each Γ level retains the same parity as N varies, but the parity of each X level alternates for successive N's. The lowest level, $0X$, has the same parity as the integer N. The parity behavior may be understood with the help of the effective mass approximation, in which an eigenfunction is the product of the bulk wavefunction at a band edge and the envelope function. The parity of the superlattice state is the product of the parity of the bulk band edge state and the parity of the envelope function. The bulk Γ state has a zero wave vector along the z-axis and, therefore, constant coefficient for each layer wave function over the GaAs region of a supercell. The superlattice Γ level, thus, has the same parity as the envelope wave function. On the other hand, the bulk X state with wave vector $(0, 0, a^*)$ has an alternating ± 1 as coefficients of the layer wave function in the AlAs region. In the AlAs region with M layers, the ratio of the coefficients of the layer function on the two interface As planes is $(-1)^M$. Thus, for the even parity envelope functions of the $(2n).X$ levels, the parity of the state is the same as that of M and, for odd parity envelope functions of the $(2n+1).X$ levels, the parity of the state is opposite to that of M. Thus, the parity behavior of the X levels shown in Fig. 12 is explained.

At $N = 16$, the crossing of the 1Γ level and the $4X$ level results in a degeneracy because the difference in parity forbids any mixing. The lowest level anti-crossing occurs at $N = 12$ (34 Å) which agrees with the observed (and expected from EMA) GaAs thickness of type II to type I superlattice transition.[50]

5.5. Valley-Mixing Between X_x and X_y

The possibility of mixing between the X_x and X_y valleys was first pointed out by Ting and Chang[54] by projecting the X points onto the interface plane. Here we shall take a more general view of the superlattice Brillioun zone.[45] The lowest conduction bands of bulk GaAs and AlAs along $a^*(1, 0, f)$ where $0 \le f \le 1$, i.e. X_x-W-X_y, have end points at X_x and at $a^*(101)$ which is connected to $a^*(010)(X_y)$ by an fcc reciprocal lattice vector. The superlattice potential mixes the two valleys and can split the valley degeneracy unless forbidden by symmetry.

The symmetry of the state with wave vector $(a^*, 0, q)$, $0 \le q \le c^*$, depends on N and M, the number of GaAs and AlAs layers in a period:

Case I. N and M both even: If we adopt the numbering system of the irreducible representations[51] of the bulk Δ for the point group of $\overline{V}$, the states of symmetry $\overline{V}_1$ and $\overline{V}_2$ correspond respectively to the mixtures $X_x \pm X_y$, as can be seen, for example, from the tight-binding wave functions. The superlattice potential causes the splitting, as shown in Fig. 13(a), from the tight-binding calculation in Ref. 45.

Case II. N and M both odd: The same two basis sets given by $X_x \pm X_y$ now have symmetry $\overline{V}_4$ and $\overline{V}_3$, respectively. The difference is due to the change of origin from As in Case I to Al in the present case. Under an inversion J, these states transform into each other. Thus, these subbands are doubly degenerate. This is compatible with the double degeneracy at the end point of $\overline{M}_5$. This is borne out by the calculation for the 7/11 superlattice shown in Fig. 13(b).

Case III. N odd and M even: The subband structure is illustrated by the 7/10 superlattice in Fig. 13(c). The general point $\overline{\Gamma}$ has only one non-trivial symmetry operation, the two-fold rotation about the z-axis. Compatible with the bulk X_1 is the even representation $\overline{\Gamma}_1$. The end points are $\overline{X}$ and $\overline{Y}$ which have the same symmetry by the tetragonal rotation S_{4z}. Thus, the subbands are symmetrical about the mid point $\overline{W}$. The bands may be thought of as ones arising from the X_x and X_y valleys crossing at $\overline{W}$ where the valley mixing splits the bands by degenerate perturbation theory. Actually, at the end points, there is a certain amount of mixing, but not of equal strength.

Case IV. N even and M odd: The states now have symmetry $\overline{T}_2$. The behavior is qualitatively similar to Case III except that the splitting is smaller, as shown in Fig. 13(d). The states at $\overline{W}_4$ and $\overline{W}_3$ correspond to the bulk $X_x \pm iX_y$.

5.6. Fractional Layer Numbers

The marked difference in the band structure in Fig. 13 as N or M changes is due to the change in symmetry. We consider here what effect the interface roughness would have on the band structure along $[a^*, 0, q]$. Based on the experimental observation of the interface roughness,[55] we adopt a simple model of the first Ga layer after an AlAs region being a mixture of Ga and Al atoms. The subbands are then calculated within the next-nearest-neighbor tight-binding model[45] using a simple virtual crystal approximation of x fraction of Al atoms in this interface layer. As x increases from 0 to 1, the 8/10 superlattice metamorphosizes to 7/11, as shown in Fig. 14. This is an interesting example of how interface effect may be studied from the electronic behavior. It is hoped that luminescence[46] and optically detected magnetic resonance[50] may be used to observe these states.

6. EFFECTS OF MAGNETIC FIELDS

A magnetic field, **B**, normal to the interface plane, quantizes the in-plane cyclotron motion into a set of discrete Landau levels. This feature leads to a distinctively two-dimensional property. A magnetic field parallel to the interface plane bends the electron orbits to cross the interfaces, resulting in reflection in the well and tunneling through the barrier. A parallel field is thus used to study the tunneling motion in a superlattice. To include the uniform magnetic field effect in the effective mass equation, we simply substitute the wave vector by the operator

$$k_{e,h} = \frac{1}{i}\nabla \pm \frac{e\mathbf{A}}{\hbar c}, \tag{22}$$

where **A** is the vector potential and the plus and minus signs refer to the electron and hole respectively.

6.1. Conduction Electron in Magnetic Field Normal to the Interface

For the conduction electron in a quantum well, the motion in the normal magnetic field is simple. The parabolic energy subbands in zero magnetic field are quantized into sets of Landau levels with equal spacing

$$\hbar\omega_c = \hbar eB/m^*c. \tag{23}$$

Each level has a degeneracy per unit area given by

$$D = \frac{eB}{\hbar c} = \frac{1}{2\pi R_c^2}, \tag{24}$$

where the cyclotron radius is

$$R_c = \sqrt{\hbar c/eB}. \tag{25}$$

The cyclotron frequence is proportional to B. Ideally, the density of states is a set of δ functions, but disorder scattering broadens the δ peaks and the localized states fill in the valleys. Still, the oscillatory dependence on the magnetic field of the density of states causes similar oscillations in conductivity (the Shubnikov-de Haas effect) and oscillations in magnetic susceptibility (the de Haas-van Alphen effect). In particular, the Shubnikov-de Haas period is commonly used to determine experimentally the electron density.

We need a formalism to treat the degenerate states in the same Landau level in order to further calculate impurity and electron-electron interaction effects in a strong magnetic field if we wish to study the electron self-energy (which we shall do presently) or the integral and fractional quantum Hall effect[56] (which you will hear about from other lecturers).

For the normal magnetic field, the vector potential lies in the interface plane and the wave vector operators defined in Eq. (22) satisfy the commutation relations

$$\begin{aligned} [k_{hx}, k_{hy}] &= \imath/R_c^2 \\ [k_{ex}, k_{ey}] &= -\imath/R_c^2 \\ [k_{hx}, k_{ey}] &= 0. \end{aligned} \tag{26}$$

We can define two sets of annihilation operators[6,57]

$$\begin{aligned} a_h &= k_{h+}R_c/\sqrt{2} \\ a_e &= k_{e-}R_c/\sqrt{2} \end{aligned} \tag{27}$$

and their Hermitian conjugates, the creation operators, obeying the usual boson commutation relations.

It is straightforward to show that the conduction effective Hamiltonian depends only on the electron operators a_e and $a_e^\dagger$ which, therefore, serve to lower or raise the state to another Landau level. The states in the nth Landau level may be written as

$$|n, m> = \frac{1}{\sqrt{n!m!}} a_e^{\dagger n} a_h^{\dagger m} |0, 0>, \tag{28}$$

where the non-zero integer m classifies all the degenerate states in the same Landau level and the ground state $|0, 0>$ has for instance the wave function

$$\frac{1}{\sqrt{2\pi}} \exp^{-r^2/4R_c^2}. \tag{29}$$

The quantum number m has a physical interpretation in that the z-component of the angular momentum for state $|n, m>$ is $n - m$ in units of $\hbar$ since the z-component of the angular momentum operator is given by

$$L_z = a_e^\dagger a_e - a_h^\dagger a_h. \tag{30}$$

Thus, $a_e^\dagger$ and a_h raise the angular momentum quantum number and a_e and $a_h^\dagger$ lower it. These states form a convenient basis set for many-body calculations and have also been used for magneto-excitons.[58]

6.2. Valence Holes in a Magnetic Field Normal to the Interface

For holes in a magnetic field normal to the interface, the mini $k.p$ method also serves the dual purposes of computing Landau levels and visualizing them. The $B = 0$ and $k = 0$ states are used as the basis set. For a magnetic field normal to the interface, the diagonal terms of the Luttinger Hamiltonian yield four sets of evenly spaced Landau levels with well-defined m_J. The off-diagonal terms provide a mixture of m_J states for each Landau level, thus changing its energy value. Figure 15 shows the typical resulting set of Landau levels.

The in-plane motion can be expressed in terms of the usual harmonic functions $u_n(x, y)$, where n is the Landau level index. $k_{h\pm}$ are the raising and lowering operators for u_n. In the cylindrical gauge, $\mathbf{A} = \mathbf{r}\times\mathbf{B}/2$, u_n can be associated with the azimuthal angular momentum eigenstates, as shown in the last section. In the cylindrical approximation of the Luttinger Hamiltonian, the envelope function is of the form[8]

$$(\psi_{3/2}(z)u_\ell, \psi_{1/2}(z)u_{\ell+1}, \psi_{-1/2}(z)u_{\ell+2}, \psi_{-3/2}(z)u_{\ell+3}). \tag{31}$$

All four components of the wave function must have the same $m_J + n$ from total angular momentum conservation. The $k.p$ mixing has two consequences: (1) The field dependence is non-linear. (2) The spacing between Landau levels is uneven. In fact, some levels do not even order monotonically with the index n.

6.3. Conduction Electron in a Magnetic Field Parallel to the Interface

Figure16 shows the magnetic field configuration relative to the superlattice. The growth axis of the superlattice is again taken to be the z-axis. The magnetic field **B** is along the x-axis. The vector potential in the Landau gauge is in the y direction: $\mathbf{A} = B(0, -z, 0)$. In the semiclassical picture, the cyclotron orbits can be centered in the well or in the barrier. The latter orbit involves tunneling through the potential barrier and, therefore, resonance of such orbits can yield information on the barrier.[35]

The semiclassical notions can be made more rigorous. For the reasons given in Sec. 4.2, a four-band model, Eq. (13), is used for the effective Hamiltonian. In a finite field, the energy subbands can still be expressed in terms of a two-dimensional wave vector (k_x, k_y) as quantum numbers[59] since the translational symmetry in the interface plane is preserved. In the Landau gauge,

$$\mathbf{A} = B(0 - z, 0). \tag{32}$$

From Eq. (22), where k_y occurs in Eq. (13), now $k_y - z/R_c^2$ takes its place. The quantum number k_y also gives the center of the cyclotron orbit along the z-axis, $R_z = k_y R_c^2$, which can be used as the quantum number instead of k_y.

Since the magnetic subband states of interest in the tunneling cyclotron resonance experiment lie close to the bottom of the GaAs well, we can carry out an expansion in $\epsilon = E - V_w - \Delta_w$, as explained in Sec. 4.2. A calculated magnetic subband at 10T is shown in Fig. 17. If B is measured in Teslas we have $R_c = (256.56/\sqrt{B})\mathring{A}$. For example, at $B = 10T$, $\ell = 81\mathring{A}$. Since the extrema of the subbands as functions of R_z occur at the centers of the wells or barriers, from the absorption spectra with thermal occupation of the lower subbands we can deduce the transition energies between some pairs of the extrema of the subbands. The absorption spectra are dominated by barrier-bound resonances.

They correspond to transitions between states whose guiding centers for the cyclotron orbits lie in the middle of the barrier. In Fig. 18, we compare the calculated transition energy with the position of the dominant peak in the absorption spectra as a function of the magnetic field strength. We note that the agreement between the calculation from the renormalized effective-mass and experiment is much better than that of the one-band EMA. The renormalized mass in the barrier, which is smaller than the AlAs conduction band effective mass, yields higher transition energies than the simple EMA. This improvement is independent of any uncertainty in the well and barrier width. This confirms our previous argument that the tunneling decay wave vector for energy deep in the gap should be treated by a two-band model including conduction-valence band interaction rather than by the parabolic approximation of the conduction band.

7. ELECTRON SELF-ENERGY EFFECTS IN A DOPED QUANTUM WELL

As an example, consider the effect of the two dimensional Fermi sea created by modulation doping in the AlGaAs barriers bounding (with spacers) a GaAs well. A conduction electron or a valence hole moves in an effective potential due to interaction with the other electrons in the Fermi sea. The effective potential, called the self-energy, contains three terms, the electrostatic potential due to the charge distribution of the electrons, the exchange and correlation terms. The latter two are non-local and the last is energy dependent. The interaction effects are stronger than in a three dimensional system because of the quantum well confinement. In the zero magnetic field case, the theory of the self-energy in the quantum well[60] is not very different from the three dimension case. The case of strong magnetic field[61,62] is more interesting for several reasons. One is the unusual magnetic field dependence, which can be checked against experiment.[63,64] The other is that because of the isolated Landau levels, the electron-impurity interaction, which provides the

level broadening, is also important. Thus, we have to deal with the intricate problem of electron-electron interaction in the presence of impurity.

7.1. The Interaction Hamiltonian

We use the model of an interacting Fermi sea in a conduction subband of Landau levels in the presence of impurities. In order to study also the hole self-energy, we allow for a single hole in a valence Landau level which interacts with the conduction electrons.[61] With the magnetic field **B** normal to the interfaces, we choose the symmetric gauge, $\mathbf{A} = B/2(-y, x, 0)$. We take from Sec. 6.3 the single-particle Landau states $|nmj\rangle$ where n is the Landau level quantum number, $n - m$ is the azimuthal angular momentum, $j = e$ for the lowest conduction subband which contains the electron Fermi sea for the n-doped quantum well, and $j = h$ for the highest valence subband. The effective Hamiltonian is chosen to consist of four terms:

$$H = H_0 + H_e + H_h + H_{\rm i} \quad . \tag{33}$$

The first term contains the single-particle terms for the conduction electrons and valence holes:

$$H_0 = \sum_{n,m} E_n^e a_{nm}^+ a_{nm} + \sum_{n,m} E_n^h b_{n,m}^+ b_{n,m} \quad , \tag{34}$$

where

$$E_n^j = (E_g/2) + \hbar\omega_{cj}(n + 1/2). \tag{35}$$

For simplicity, the spin-splitting is neglected and the spin degeneracy is understood. The next two terms are, respectively, the Coulomb interaction terms among the conduction electrons and between the electrons and holes, given by

$$H_e = \frac{1}{S}\sum_q \sum_{n_1,m_1} \sum_{n_2,m_2} \sum_{n_3,m_3} \sum_{n_4,m_4} V^{ee,m_1,m_2,m_3,m_4}_{n_1,n_2,n_3,n_4}(q) a^+_{n_1 m_1} a^+_{n_2 m_2} a_{n_3 m_3} a_{n_4 m_4}, \tag{36}$$

and

$$H_h = -\sum_q \sum_{n_1,m_1} \sum_{n_2,m_2} \sum_{n_3,m_3} \sum_{n_4,m_4} V^{eh,m_1,m_2,m_3,m_4}_{n_1,n_2,n_3,n_4}(q) a^+_{n_1 m_1} b^+_{n_2 m_2} b_{n_3 m_3} a_{n_4 m_4}, \tag{37}$$

where $V^{ej,m_1,m_2,m_3,m_4}_{n_1,n_2,n_3,n_4}$, for $j = e, h$, is the matrix element of the Coulomb potential $V(q) = 2\pi e^2/\epsilon_0 q$, ϵ_0 being the dielectric constant of the background material. We refer to Ref. 61 for explicit expressions for these matrix elements.

7.2. Screening

The Coulomb interaction is screened by the conduction electrons. The dielectric function $\epsilon(q, i\omega)$ can be expressed in terms of the proper polarization $\Pi(q, i\omega)$:

$$\epsilon(q, i\omega) = 1 - F^{ee}(q)V(q)\Pi(q, i\omega). \tag{38}$$

We use the RPA for the proper polarization in the sense that it contains no Coulomb interaction. It does, however, contain the impurity effects in the one-particle propagator, as shown in the upper part of Fig. 19, and in the ladder diagrams as in the lower part of the figure.[65] By including the impurity scattering in both the vertex and in the self-energy, the Ward identity is satisfied within the self-consistent Born approximation.

We shall see below that the most important part of the screening effect in the self-energy is $\epsilon(q, 0)$. We can concentrate on the solution for the static dielectric function $\epsilon(q, 0)$, an approximation for which, valid in the small q limit, is given in the form:

$$\epsilon(q, 0) = 1 + q_s/q - F^{ee}(q)V(q)\Pi_{nd}(q, 0). \tag{39}$$

The screening parameter q_s in Eq. (40) is given by

$$q_s = 2\pi e^2 D(E_F)/\epsilon_0, \tag{40}$$

where $D(E_F)$ is the density of states at the Fermi level. The non-diagonal part of the polarization, $\Pi_{nd}(q, 0)$, consisting of the inter-Landau level excitations, i.e. $n \neq n'$ terms, is of higher order in q than the diagonal part. It may, therefore, be evaluated in the simple bubble approximation, neglecting the impurity vertex correction. In a high magnetic field the density of states oscillates with the variation of field strength, and, thus, the

screening effect has also an oscillatory field dependence,[65] showing alternating metal-like and insulator-like behavior.

7.3. Electron and Hole Self-Energies

The self-energy $\Sigma^j(n)$ at level n due to Coulomb interaction can be evaluated as in the zero magnetic field case neglecting the recoil energy of the particle (the so-called quasi-static approximation[60]). The self-energy then has two terms, screened exchange and Coulomb-hole:

$$\Sigma^j(n) = \Sigma^j_{ex}(n) + \Sigma^j_{ch}(n), \tag{41}$$

$$\Sigma^e_{ex}(n) = -\sum_{n_1}\sum_q \frac{V^{ej}_{nn_1}(q)}{\epsilon(q,0)}\nu^e_{n_1}, \tag{42}$$

$$\Sigma^e_{ch}(n) = \frac{1}{2}\sum_{n_1}\sum_q V^{ee}_{nn_1}(q)\left(\frac{1}{\epsilon(q,0)}-1\right), \tag{43}$$

$$\Sigma^e_{ch}(n) = \frac{1}{2}\sum_{n_1}\sum_q \frac{V^{eh}_{nn_1}(q)^2}{V^{ee}_{nn_1}(q)}\left(\frac{1}{\epsilon(q,0)}-1\right), \tag{44}$$

where the abbreviated Coulomb matrix element is given by

$$V^{ej}_{nn_1}(q) = V^{ej,0,0,0,0}_{n,n_1,n,n_1}. \tag{45}$$

Note that, while $\Sigma^e_{ex}(n)$ depends explicitly on the conduction electron occupation, $\Sigma^j_{ch}(n)$ depends on the conduction electron occupation only indirectly through the dielectric screening. Since we have neglected the exchange interaction between the conduction electron and the valence hole and since the valence hole density due to photon excitation is taken to be much less than the electron density, the valence hole self-energy has a negligible exchange term and has only the Coulomb-hole term, $\Sigma^h_{ch}(n)$. From the explicit expressions of the dependence of the screened exchange and Coulomb-hole terms on the dielectric function, it is clear that, following the oscillatory magnetic field dependence of the screening parameter, the two self-energy terms will oscillate as functions of the magnetic field, albeit out of phase. The two terms in the conduction electron self-energy tend to cancel each

other out, but the valence hole self-energy, having only the Coulomb-hole term, gives the dominant oscillatory behavior in the pair total energy. In Fig. 20, we show the magnetic field dependence of the screening parameter q_s, the screened exchange term $\Sigma^e_{ex}(0)$ and the Coulomb-hole term $\Sigma^e_{ch}(0)$ for the conduction electron. An electron density of $4\times10^{11}cm^{-2}$ and a well width of 200 Å are used in this calculation. The screening parameter q_s, being proportional to the density of states, has maxima at the Landau filling factor ν = odd integer, where the highest occupied spin-degenerate Landau level is half-filled. Here we use the Gaussian type density of states for the Landau levels,[65]

$$D_n(E) = 1/\pi\ell^2\sqrt{(2/\pi)}/\Gamma exp\{-2(E-E_n)^2/\Gamma^2\}, \tag{46}$$

where Γ, the level width due to impurity scattering, is proportional to $\sqrt{B}$,

$$\Gamma/\hbar\omega_c = \alpha/\sqrt{B}. \tag{47}$$

Here, α is a parameter, taken to be 0.5 in Fig. 20.

7.4. Comparison with Experiment

In Fig. 21 the calculated transition energies between conduction and valence band Landau levels as functions of the magnetic field (solid lines) are compared with the experimental energies[64] for $InP/In_yGa_{1-y}As$. The phase of oscillation of the transition energy as the magnetic field varies, which has maxima around Landau filling factor $\nu = 2, 4, \ldots$, are in good agreement with experiment. The phase of oscillation coincides with that of the hole self-energy. This confirms our argument given above on the relative importance of various self-energy terms. The exciton effect is important but not pronounced.[61]

8. PHOTOLUMINESCENCE IN UNDOPED AND DOPED QUANTUM WELLS

The photo-luminescence process consists of three steps (Fig. 22): (1) Excitation: Light is absorbed producing electron-hole pairs or excitons. (2) The electrons and holes thus produced relax to lower energy states or to exciton states. (3) The electron-hole pair or exciton recombines giving out luminescent light. When the excitation light frquency is swept and luminescence is measured at a fixed frequency, usually that of the lowest exciton line or band edge, the intensity as a function of the excitation light frequency is called the photoluminescence excitation spectrum (PLE). If the excitation light frequency is fixed, the intensity of emitted light as a function of the emitted light frequency is called the photoluminescence spectrum (PL). In both the excitation and luminescence spectra, the heavy and light hole excitons are well resolved.

Control of the polarization of the excitation light to be absorbed by the quantum well and measurement of the emitted light in different polarizations yield further information on the state of the electron-hole pair. Since the conduction electron state is simple, the nature of the valence subband states may be deduced from such measurements. For the quantum wells, two configurations of polarization measurements have been carried out: (1) back scattering: where a circularly polarized light is incident normally on the quantum well and polarization of light emitted near the normal is measured[66]; (2) wave-guided: where the quantum well acts as a wave guide such that the emitted light along the interface plane is measured for polarization normal to the plane and parallel to the plane.[67]

8.1. Selection Rules

In the effective mass approximation, the transition matrix element between a conduction subband state (e, s) and a valence subband state component (h, m_J) is given by

$$< e, s|\mathbf{p} \cdot \mathbf{A}|h, m_J >< f_{e,s}|f_{h,m_J} >, \tag{48}$$

a product of the momentum matrix element of the Bloch waves at the band edges and the overlap between the envelope functions, where $s = \pm 1/2$ is the z-component of the electron spin and $m_J = 3/2, 1/2, -1/2, -3/2$ is the hole angular momentum. Evaluation of the momentum matrix element between the Bloch waves is straightforward. For different light polarization, the resulting set of selection rules relating s and m_J can be cast in terms of the z-component angular momentum conservation:

$$s - m_J = m_{ph} \tag{49}$$

if we assign the photon angular momentum m_{ph} values ± 1 for $\sigma_\pm$, right and left circularly polarized light about the z-axis, normal to the interface plane and the value zero for the π, polarization along the z-axis. With the help of the selection rules, one can in principle deduce from the measured polarization spectra the heavy and light hole nature of the valence states.

8.2. Polarization Spectrum in the Back-Scatter Configuration

Consider the configuration in which both the excitation light and the emitted light are measured at normal incidence,[66] as sketched in Fig. 23. The incoming photon is circularly polarized in the right handed sense (σ_+). The fraction difference of emitted intensity of σ_+ light is defined as the polarization:

$$P = \frac{I_+ - I_-}{I_+ + I_-} \tag{50}$$

In general, the spin relaxation time of the electron is much longer than both the momentum relaxation time and the recombination time so that the spin of the excited electron is taken as unchanged. The hole spin relaxes very quickly to the lowest state so that, in the quasi-equilibrium just before recombination, hole spin is randomized because of the four component mixing of the valence subbands. These assumptions lead to a qualitative explanation[68] of the polarization spectrum in the undoped quantum wells in terms of the valence band structure. Predominantly -1/2 (spin down) electrons will be produced by excitation from heavy holes with $m_J = -3/2$. (The 3/2 state cannot be excited by σ_+ light according to the angular momentum conservation rule.) After relaxation, the electron retains its down-spin while all m_J values of holes are available. Recombination of the -1/2 spin electron with -3/2 heavy holes yields a σ_+ photon and recombination of the -1/2 spin electron with +1/2 light hole yields a σ_- photon. The spin reversal of polarization,[66] shown in Fig. 24c, from heavy-hole to light-hole excitons, is thus qualitatively explained.

The same assumption of complete hole spin relaxation in an n-doped quantum well, in which a Fermi sea of electrons of both spins is present, leads to a featureless polarization spectrum, in contradiction to experiment.[66] (See Fig. 24b). The spin polarization of the electron Fermi sea by the photo-excited valence hole through an exchange interaction was invoked to explain the polarization reversal at the $2h \rightarrow 2c$ in going from the undoped to the n-doped wells.[69] We[70] have undertaken a study of the hole relaxation processes after photo-excitation. The results contradict the common assumption of complete spin relaxation of the photo-excited holes.

We examine the hole relaxation by emission of acoustic phonons in both undoped and doped wells and by shake-up[71] of the electron Fermi sea in the n-doped wells. While these processes provide *per se* only momentum and energy relaxation, the different mixings of spin components in different hole states through the $k \cdot p$ terms lead to hole spin relaxation. Since the intrinsic hole spin relaxation is much slower than the momentum relaxation, the

hole spin relaxation is incomplete prior to radiative recombination. While in the bulk solid the hole spin seems to be quite well relaxed, uniaxial stress in bulk GaAs tends to reduce hole spin relaxation.[72] Quantum well confinement appears to play a similar role as the uniaxial stress.

8.2.1. Parity of Hole States

Since the spin components are mixed in a valence state, what takes the place of the spin quantum number in momentum relaxation? In a symmetric quantum well, we find the parity to be a good quantum number. The z-dependence of the four components of the envelope has definite parity, $p_m = \pm 1$, for the m-th component. (In this section, m_J is abbreviated to m.) From the structure of the Luttinger Hamiltonian, Eq. (2), the parity of the four components of the envelope wave function must alternate. Thus, we can define a parity p for each hole state:

$$p_m = p(-1)^{\frac{1}{2}-m}. \tag{51}$$

An important example is the top of the valence subband at zero wave vector where there are two pure spin $\pm 3/2$ states. The one with pure $+3/2$ spin would be even parity and the one with $-3/2$ spin would have odd parity by our definition.

8.2.2. Relaxation Processes

The conduction electron promoted from the valence band by the excitation light relaxes to the lowest available conduction subband state in a time much shorter than the electron spin relaxation time τ_s or the electron-hole recombination time τ_r.[73] The hole-acoustic phonon scattering through the deformation potential is given by the strain Hamiltonian[74] of the same form as the Luttinger Hamiltonian. The acoustic phonons in the quantum well are classified into even and odd parity phonons. It is then easy to deduce from the parity of

the strain tensor that phonon scattering either preserves or changes the parity of the hole state and that the parity conserving hole momentum relaxation time, τ_+, is shorter than the parity changing counterpart, τ_-. The spin relaxation then comes about because the initial and final hole states are made up of different mixtures of the spin components which are determined by the calculated subband structure. At the top of the valence subbands, the hole spin relaxation time is taken to be roughly the same as the electron one, τ_s, much longer than $\tau_\pm$.

For the n-doped well, the hole can also relax by shaking up the electron Fermi sea. While we shall see that the shake-up process is important for the emission with z-polarization in the wave guide configuration,[71] it is less than 10% of the simple recombination with $\sigma^\pm$ polarizations. While it strengthens somewhat the parity conserving hole relaxation, the Auger process is not as important as the acoustic phonon scattering.

8.2.3. Spin Populations

The numbers of electrons and holes of each spin species produced by the excitation light at a given energy are calculated by the simple optical transition. There are four types of transitions excited by the σ_+ light at a given energy interval from hole component with spin and parity (m, p_m) to electron with spin and parity (s, p_s): (a) $(-3/2, +1) \rightarrow (-1/2, +1)$; (b) $(-3/2, -1) \rightarrow (-1/2, -1)$; (c) $(-1/2, +1) \rightarrow (1/2, +1)$; (d) $(-1/2, -1) \rightarrow (1/2, -1)$. For the incident light with σ^+ polarization, the generation rate of electrons with spin $s = \pm\frac{1}{2}$ are given by:

$$G^e_{-\frac{1}{2}} = (a) + (b). \tag{52}$$

$$G^e_{\frac{1}{2}} = (c) + (d). \tag{53}$$

The generation rate of holes of parity $p = \pm 1$ is given by:

$$G^h_{-1} = (a) + (d), \tag{54}$$

$$G^h_{+1} = (b) + (c). \tag{55}$$

The relation of the parity of each component to the parity of the hole state, Eq.(51), is used.

With carrier generation rates and the relaxation times defined above, we set up the rate equations[75] and solve for the steady state spin populations. In a p-doped quantum well, the presence of equal spin populations of holes means that the luminescence polarization is determined by the electron spin polarization:

$$\mathcal{P}_p = \frac{G^e_{-\frac{1}{2}} - G^e_{\frac{1}{2}}}{G^e_{-\frac{1}{2}} + G^e_{\frac{1}{2}}} \frac{\tau_s}{\tau_s + \tau_r}. \tag{56}$$

Similarly, in the n-doped well, the luminescence polarization is determined by the hole spin population:

$$\mathcal{P}_n = \frac{G^h_{-1} - G^h_1}{G^h_{-1} + G^h_1} \frac{\tau_- - \tau_+}{\tau_- + \tau_+} \frac{\tau_s}{\tau_s + \tau_r}. \tag{57}$$

In the undoped well, the emission intensity depends on the lesser of the numbers of electrons and of holes available for recombination satisfying the angular momentum selection rule. Thus, the polarization is given by

$$\mathcal{P}_u = \frac{\min(n^e_{-\frac{1}{2}}, n^h_{-1}) - \min(n^e_{\frac{1}{2}}, n^h_1)}{\min(n^e_{-\frac{1}{2}}, n^h_{-1}) + \min(n^e_{\frac{1}{2}}, n^h_1)}. \tag{58}$$

8.2.4. Polarization Spectra

Figure 24 shows, in order, the calculated polarization spectra for a p-doped, an n-doped, and an undoped quantum well in comparison with experiment. The two ratios, τ_r/τ_s and τ_+/τ_-, are taken to be 0.12 and 0.46 to fit the magnitude of observed polarization[66] in the p-doped and n-doped quantum well, respectively. The same values are then used for the undoped well spectrum. The marked features are related to the valence to conduction subband transitions. All these features arising out of incomplete hole spin relaxation are

in qualitative agreement with observation[68] and the energies at which they occur are in quantitative agreement, for undoped and doped quantum wells.

8.3. Luminescence Polarization in the Waveguide Configuration

Figure 25 shows the experimental set-up.[67,71] The multiple quantum well structure contains undoped AlGaAs spacer layers which separate the doped AlGaAs layers from the GaAs layers with the electrons, thus increasing the electron mobility. The excitation light is incident normal to the layers (along the z-axis). The emitted light is wave-guided along the interface planes of the quantum well (along the y-axis) and its intensity is measured in two polarizations, along the normal (z-axis) and parallel to the interfaces (along x-axis).

8.3.1. Simple Recombination Processes

In step (3) of the luminescence process, the simple recombination consists in the de-excitation of an electron from the Fermi sea of the n-doped quantum well to a hole in the valence subband emitting a photon. The polarization of the emitted light can be determined with the help of the selection rule based on angular momentum conservation, Eq. (49).

Since the top heavy hole subband ($1h$) lies above the top light hole subband (1ℓ), we expect the intensity of the x-polarization, I_x, to start at the conduction subband $1c$ to $1h$ threshold, E_{ch}. Since the transition from spin $\pm 1/2$ conduction band states to the $\pm 3/2$ heavy hole states cannot result in zero angular momentum photons, the z polarization spectrum, I_z has to start at zero intensity from the threshold E_{ch} and grows gradually as the heavy hole subband $1h$ acquires more light hole mixing as the photon energy increases. I_z has a sudden increase at the threshold $E_{c\ell}$ when the electron to light hole transition comes into play. Figure 26 shows the calculated emission spectra for the two polarizations from the one-particle transitions. Contrary to the expectation based on the simple recombination

processes, the observed I_z spectrum starts at the same threshold as the I_x spectrum (Fig. 27a). The intensity at the threshold cannot be explained by the gradual increase due to the m_J mixing of the $1h$ subband.

8.3.2. Shake-Up Processes

A number of causes for the m_J mixing at the top of the $1h$ subband have been examined: k-linear term due to deviation of GaAs from the diamond lattice, asymmetry of the quantum well due to the different quality of the interfaces as a consequence of the growth process of the quantum wells, impurity, strain, invalidity of the effective mass approximation and the many-body effect in the luminescence process.[67,71] With the exception of the last one, these yield I_z one order of magnitude too small at the threshold E_{ch}.

Consider a single relaxed hole as the initial state before light emission. As is well known, the Fermi sea of electrons reacts to the presence of the hole. The process is entirely analogous to the soft X-ray emission in metals.[76] The excitation of the Fermi sea consists of electron-hole pairs and plasmons. The lowest order shake-up processes are given by[77] the Feynman diagrams, Figs. 28 c, d, e, and g. The shake-up represented by diagram c or its exchange counterpart d takes place in two steps, as described by Fig. 28b: (1) The relaxed hole initially at state k of the valence subband excites an electron-hole pair k_1 and k_2 from the conduction subband Fermi sea through the screened Coulomb interaction. The hole recoils to state k' in the same or a different valence subband. (2) A conduction electron at k' recombines with the hole at k' emitting a photon. Thus, even if the initial hole state k is dominated by the $3/2$ component, the intermediate state k' provides polarization mixing for the light emission.

Figure 28e is the diagrammatic representation of the initial-state interaction or the excitonic effect. The process is described pictorially by Fig. 28f, in which a hole excites a conduction electron of the same momentum out of the Fermi sea and then recombines with

the same electron. Such a process produces no additional polarization mixing since the sum of all the electron-hole pairs at k' before recombination cancels out the polarization mixing of the individual pair.

Figure 28g has the same vertex structure as Fig. 28e, but the difference is in the retarded screened Coulomb interaction. The process has an intermediate state like that in Fig. 28b rather than Fig. 28f.

The lowest order diagram c diverges at the band edge,[78] and higher order terms have to be summed.[79] I constructed a simple formula for the shake-up effect[71] which takes into account the phase space of the scattering events but not the state dependence of the interaction matrix element or the energy denominators. The emission intensity in the α polarization is given by

$$I_\alpha(\omega) = \sum_{jk} [M_\alpha(jk) + \lambda \langle M_\alpha(j'k') \rangle_{j'k'}] e^{-E_{jk}/\Gamma} \delta(E_{ck} - E_{jk} - \hbar\omega). \tag{59}$$

$M_\alpha(jk)$ is the single electron transition probability from the conduction state ck to the valence band state jk with momentum $\mathbf{k}$ at polarization α, i.e. square of the expression (48). The exponential factor would, in the non-interacting approximation, be the thermal distribution of the initial hole state in quasi-equilibrium with temperature Γ. To fit the high energy side of the I_z spectrum, Γ is about 20K. Although the hole temperature could be higher than the lattice temperature which is kept at 2K, 20K is unreasonably high. Our justification of the large Γ is then not the initial hole temperature but the broadening of the initial hole spectral density due to self-energy effects (Fig. 28a) by the same processes as the shake-up. The second term in the square bracket on the right hand side of the formula is an average of the one-electron recombination processes over the Fermi sea, approximating the second step of the shake-up process.

The factor λ is a measure of the strength of the electron hole interaction and is obtained by fitting the peak height of the shake-up portion of the I_z spectrum (Fig. 27a) in the region

of 0-5 meV above threshold below the onset of the electron light hole recombination. With two adjustable parameters Γ and λ, the spectra for two polarizations are well accounted for (see Fig. 27a).

The validity of the model is further confirmed by its ability to account for the stress[71] and magnetic field dependence for both polarizations without further changing the values of λ and Γ.

8.3.3. Stress

Uniaxial stress along the normal (001) and in the (110) plane add terms to the Luttinger Hamiltonian for the holes[6] given by

$$\Delta \begin{bmatrix} -1 & & & \\ & 1 & & \\ & & 1 & \\ & & & -1 \end{bmatrix}$$

$$\Delta \begin{bmatrix} +1 & i\alpha & & \\ -i\alpha & -1 & & \\ & & -1 & i\alpha \\ & & -i\alpha & 1 \end{bmatrix} \tag{60}$$

where the strain $\Delta > 0$ represents compression. The (001) stress preserves the tetragonal symmetry of the quantum well. It changes the spacing between the $1h$ and 1ℓ subbands without changing the m_J symmetry of the states at $k = 0$. The resulting subband structure is shown in the middle panel of Fig. 29. The closing of the 1ℓ band to the $1h$ band increases the single particle recombination portion of the I_z spectrum relative to the shake-up portion, as is evident in both theory and experiment in the middle panels of Fig. 27. The discrepancy of the magnitude of stress between experiment and theory may be attributed to the difficulty in measuring the stress and the inaccuracy of calculated stress dependence

of the subbands.

The (110) stress distorts the tetragonal symmetry about the normal to the interface plane. Even though the stress increases the spacing between $1h$ band and 1ℓ band (the right hand panel of Fig. 29), it mixes strongly the different m_J components. As a result, the single particle recombination processes are dominant in the I_x spectrum from the "heavy hole band," $1h$. Hence, the spectra in both polarizations are similar in form, as borne out by theory and experiment (the right hand panels of Fig. 27).

ACKNOWLEDGEMENT

My part of the work described above is supported by the U.S. National Science Foundation, Grant No. DMR 88-15068.

REFERENCES

1. See for example, *Molecular Beam Epitaxy and Heterostructures* (L.L. Chang and K. Ploog, eds.), M. Nijhoff, Dordrecht, The Netherlands (1985).

2. L.J. Sham and M. Nakayama, *Phys. Rev. B* **20**, 734 (1979).

3. E.O. Kane, in: *Semiconductors and Semimetals*, Vol.1, *Physics of III-V Compounds* (R.K. Willardson and A.C. Beer, eds.) Academic Press, New York (1966), p. 75.

4. S. White and L.J. Sham, *Phys. Rev. Lett.* **47**, 879 (1981).

5. H.L. Stormer, R. Dingle, A.C. Gossard, W. Wiegmann, and M.D. Sturge, *J. Vac. Sci. Technol.* **16**, 1517 (1979).

6. J.M. Luttinger, *Phys. Rev.* **102**, 1030 (1956). K. Suzuki and J. Hensel, *Phys. Rev. B* **9**, 4184, and 4219 (1974).

7. S.S. Nedorezov, *Fiz. Tverd. Tela* **12**, 2269 (1970). [*Sov. Phys. Solid State* **12**, 1814 (1970)].

8. D.A. Broido and L.J. Sham, *Phys. Rev. B* **31**, 888 (1985).

9. J. Schulman and Y.C. Chang, *Phys. Rev. B* **31**, 2056 (1985).

10. M. Altarelli, *J. Lumin.* **30**, 472 (1985).

11. T. Ando, *J. Phys. Soc. Jpn.* **54**, 1528 (1985).

12. S.-R. Eric Yang, D.A. Broido, and L.J. Sham, *Phys. Rev. B* **32**, 6630 (1985).

13. D.A. Broido and L.J. Sham, *Phys. Rev. B* **34**, 3917 (1986).

14. W. Kohn and L.J Sham, *Phys. Rev. A* **140**, 1133 (1965).

15. C.G. Van de Walle and R.M. Martin, *Phys. Rev.* **B35**, 8154 (1987).

16. A. Baldereschi, S. Baroni, and R. Resta, *Phys. Rev. Lett.* **61**, 734 (1988).

17. J. Tersoff, *Phys. Rev.* **30**, 4874 (1984).

18. W.R.L. Lambrecht and B. Segall, *Phys. Rev. Lett.* **61**, 1764 (1988).

19. R. Dingle, in: *Festkörperprobleme XV* (H.J Queisser, ed.), Pergamon-Vieweg, Braunschweig (1975), p. 21.

20. R.C. Miller, A.C. Gossard, D.A. Kleinman, and O. Munteanu, *Phys. Rev. B* **29**, 3740 (1984).

21. R.C. Miller, D.A. Kleinman, and A.C. Gossard, *Phys. Rev. B* **29**, 7085 (1984).

22. D.J. Wolford, in: *Proc. 18th International Conference of Physics of Semiconductors* (O. Engström, ed.), World Scientific, Singapore (1987), p. 1122.

23. A. Zunger, *Phys. Rev. Lett.* **54**, 848 (1985).

24. J.M. Langer and H. Heinrich, *Phys. Rev. Lett.* **55**, 1414 (1985).

25. A.D. Katnani and R. S. Bauer, *Phys. Rev.* **B33**, 1106 (1986).

26. M. Heiblum, M.I. Nathan, and M. Eizenberg, *Appl. Phys. Lett.* **47**, 503 (1985).

27. J. Batey and S.L. Wright, *J. Appl. Phys.* **59**, 200 (1986).

28. W.I. Wang and F. Stern, *J. Vac. Sci. Technol. B* **3**, 1280 (1985).

29. H. Okumura, S. Misawa, S. Yoshida, and S. Gonda, *Appl. Phys. Lett.* **46**, 377 (1985).

30. J. Menendez, A. Pinczuk, D.J. Werder, A.C. Gossard, and J.H. English, *Phys. Rev.* **33**, 8863 (1986).

31. G.A. Sai-Halasz, R. Tsu, and L. Esaki, *Appl. Phys. Lett.* **30**, 651 (1977).

32. B.A Wilson, *J. Quan. Electron.* **24**, 1763 (1988).

33. G. Bastard, *Phys. Rev. B* **25**, 7584 (1982).

34. W.A. Bardeen, M.S. Chanowitz, S.D. Drell, M. Weinstein, and T.M. Tan, *Phys. Rev. D* **11**, 1094 (1975).

35. G. Brozak, E.A. de Andrada e Silva, L.J. Sham, F. DeRosa, P. Miceli, S.A. Schwarz, J.P Harbison, L.T. Florez, and S.J. Allen, *Phys. Rev. Lett.* **64**, 471 (1990).

36. D.J. Ben Daniel and C.B. Duke, *Phys. Rev.* **152**, 683 (1966).

37. O. Madelung, in: *Landolt-Bornstein Numerical Data and Functional Relationships in Science and Technology*, Springer Verlag, Berlin (1987).

38. L.L. Chang, N.J. Kawai, E.E. Mendez, C. A. Chang, and L. Esaki, *Appl. Phys. Lett.* **38**, 30 (1981).

39. J.N. Schulman and T.C. McGill, *Appl. Phys. Lett.* **34**, 663 (1979).

40. Y.C. Chang, J.N. Schulman, G. Bastard, Y. Guldner, and M. Voos, *Phys. Rev. B* **31**, 2557 (1985).

41. Y.R. Lin-Liu and L.J. Sham, *Phys. Rev. B* **32**, 5561 (1985).

42. V. Korenman and H.D. Drew, *Phys. Rev. B* **35**, 6446 (1987). O.A. Pankratov, S.V. Pakhomov and B.A. Volkov, *Solid State Commun.* **61**, 93 (1987).

43. B.A. Wilson, *J. Quantum Electron.* **24** 1763 (1988).

44. L.J. Sham and Yan-Ten Lu, J. Lumin. **44**, 207 (1989).

45. Yan-Ten Lu and L.J. Sham, *Phys. Rev. B* **40**, 5567 (1989).

46. See, for example, M.D. Sturge, E. Finkman, and M.C. Tamargo, *J. Lumin.* **40**, 425 (1988). For more extensive lists of references, see Ref. 43-45.

47. G. Danan, F.R. Ladan, F. Mollot, and R. Planal, *J. Phys. (Paris) Colloq.* **48**, C5-499 (1987). M.-H. Meynadier, R.E. Nahory, J.M. Worlock, M.C. Tamargo, J.L. de Miguel, and M.D. Sturge, *Phys. Rev. Lett.* **60**, 1338 (1988)

48. D.J. Wolford, T.F. Kuech, J.A. Bradley, M.A. Gell, D. Ninno, and M. Jaros, *J. Vac. Sci. Technol. B* **4**, 1043 (1986).

49. B. Gil, P. Lefebvre, H. Mathieu, F. Mollot, and R. Planel, in: *Proc. 19th Intl. Conf. Phys. Semiconductors* (W. Zawadzki, ed.) Polish Acad. Sci., Warsaw (1988), p. 365.

50. H.W. van Kesteren, E.C. Cosman, F.J.A.M. Greidanus, P. Dawson, K.J. Moore, and C.T. Foxon, *Phys. Rev. Lett.* **61**, 129 (1988).

51. G.F. Koster, *Solid State Phys.* **5**, 174 (1957).

52. G.A. Sai-Halasz, L. Esaki, and W.A. Harrison, *Phys. Rev. B* **18**, 2812 (1978). J. Schulman and T.C. McGill, *Phys. Rev. B* **19**, 6341 (1979). H. Rücker, M. Hanke, F. Bechstadt, and R. Enderlein, *Superlattices and Microstructures* **2**, 477 (1986).

53. W. Andreoni and R. Car, *Phys. Rev. B* **21**, 3334 (1980). M.A. Gell, D. Ninno, M. Jaros, D.J. Wolford, T.F. Keuch, and J.A. Bradley, *Phys. Rev. B* **35**, 1196 (1987). Jian-Bai Xia, *Phys. Rev. B* **38**, 8358 (1988).

54. D. Z.-Y. Ting and Y.C. Chang, *Phys. Rev. B* **36**, 4359 (1987).

55. I. Umebu, S. Komiya, T. Nakamura, S.I. Mutoh, and A. Iida, *J. Phys. (Paris)* **48**, C5-41 (1987).

56. R.E. Prange and S.M. Girvin, *The Quantum Hall Effect*, Springer-Verlag, Berlin (1987).

57. A.H. MacDonald and D.S. Ritchie *Phys. Rev. B* **33**, 8336 (1986).

58. S.-R. Eric Yang and L.J. Sham, *Phys. Rev. Lett.* **58**, 2598 (1987). L. J. Sham, in: *High Magnetic Fields in Semiconductor Physics II*, (G. Landwehr, ed.) Springer-Verlag, Berlin (1989), p. 232.

59. G. Belle, J. C. Maan and G. Weimann, *Solid State Commun.* **56**, 65 (1985). J. C. Maan, *Superlattices and Microstructures* **2**, 557 (1986)

60. H. Haug and S. Schmitt-Rink, *Prog. Quantum Electron.* **9**, 3 (1984).

61. T. Uenoyama and L.J. Sham, *Phys. Rev. B* **39**, 11044 (1989).

62. S. Katayama and T. Ando, *Solid State Commun.* **70**, 97 (1987).

63. M.C. Smith, A. Petrou, C.H. Perry, J.M. Worlock, and R.L. Aggarwal, in: *Proc. of 17th Intl. Con. on the Physics of Semiconductors*, San Francisco, 1984 (D.J. Chadi and W.A. Harrison, eds.) Springer-Verlag, New York (1985). C.H. Perry, J.M. Worlock, M.C. Smith, and A. Petrou, in: *High Magnetic Fields in Semiconductor Physics* (G. Landwehr, ed.) Springer-Verlag, Berlin (1987), p. 202.

64. M.S. Skolnick, K.J. Nash, S.J. Bass, P.E. Simmonds, and M.J. Kane, *Solid State Commun.* **67**, 637 (1988).

65. T. Ando and Y. Uemura, *J. Phys. Soc. Japan* **37**, 1044 (1974).

66. R.C. Miller and D.A. Kleinman, *J. Lumin.* **30**, 520 (1985).

67. R. Sooryakumar, D.S. Chemla, A. Pinczuk, A.C. Gossard, W. Wiegmann, and L.J Sham, *Solid State Commun.* **54**, 859 (1985).

68. A. Twardowski and C. Hermann, *Phys. Rev. B* **35**, 8144 (1987).

69. A. E. Ruckenstein, S. Schmitt-Rink, and R. C. Miller, *Phys. Rev. Lett.* **56**, 504 (1986).

70. T. Uenoyama and L.J. Sham, to be published.

71. R. Sooryakumar, A. Pinczuk, A.C. Gossard, D.S. Chemla, and L.J Sham, *Phys. Rev. Lett.* **58**, 1150 (1987).

72. G. Lampel, A.N. Titkov, and V.I. Safarov, in: *Proceedings of the 14th Intern. Conf. Phys. Semiconductors* (B.L.H. Wilson, ed.) Institute of Physics, London (1978), p. 1031.

73. R.C. Miller, D.A. Kleinman, W.A. Nordland, and A.C. Gossard, *Phys. Rev. B* **22**, 863 (1980).

74. F. H. Pollak and M. Cardona, *Phys. Rev.* **172**, 816 (1968).

75. G. Lampel, *Phys. Rev. Lett.* **20**, 491 (1968).

76. L. Hedin, in: *X-ray Spectroscopy* (L.V. Azaroff, ed.) McGraw-Hill, N.Y. (1974), p. 226.

77. L.J. Sham, *J. de Physique*, **48**, C5-381 (1987).

78. A.J. Glick and P. Longe, *Phys. Rev. Lett.* **15**, 589 (1965).

79. U. von Barth and G. Grossmann, *Phys. Rev. B* **25**, 5150 (1982); see also references therein.

Table I. Symmetry properties of superlattice (N/M)

N + M	even		odd	
Bravais lattice	simple tetragonal		body-centered tetragonal	
Space group	$D_{2d}^5\,(P\bar{4}m2)$		$D_{2d}^9\,(I\bar{4}m2)$	
$\vec{k}(0 \le q \le c^*)$	notation	$\mathcal{G}_k$	notation	$\mathcal{G}_k$
$(0,0,0)$	$\bar{\Gamma}$	D_{2d}	$\bar{\Gamma}$	D_{2d}
$(0,0,q)$	$\bar{\Lambda}$	C_{2v}	$\bar{\Lambda}$	C_{2v}
$(0,0,c^*)$	Z	D_{2d}	$\bar{Z}$	D_{2d}
$(a^*,0,0)$	M	D_{2d}	$\bar{X}$	D_2
$(a^*,0,q)$	V	C_{2v}	$\bar{T}$	C_2
$(a^*,0,c^*/2)$	$\bar{V}$	C_{2v}	$\bar{W}$	S_4
$(a^*,0,c^*)$	A	D_{2d}	$\bar{Y}$	D_2
$(a^*/2,a^*/2,0)$	X	C_{2v}		C_{1h}
$(a^*/2,a^*/2,c^*/2)$	W	C_{2v}	$\bar{N}$	C_{1h}
$(a^*/2,a^*/2,c^*)$	R	C_{2v}		C_{1h}

$\mathcal{G}_k$: Point group at vector $\vec{k}$

FIGURE CAPTIONS

Fig. 1 Bulk band structure of a III-IV semiconductor, (a) without spin-orbit interaction, and (b) with spin-orbit splitting.

Fig. 2 Energy band edges in a quantum well and illustration of modulation doping.

Fig. 3 Electron subbands and density of states in a quantum well.

Fig. 4 Valence subbands in a GaAs/AlGaAs quantum well.

Fig. 5 Effective mass picture across an interface.

Fig. 6 Conduction and valence band edge alignment in three types of superlattices.

Fig. 7 Bulk energy bands for real (solid lines) and imaginary (dashed lines) wave vectors.

Fig. 8 (a) Subbands in a type II superlattice. (b) Optical gap as a function of equal InAs and GaSb layer width. The solid lines are for the two-band model and the dotted lines for the one-band model for the band overlap values of 150 meV (upper) and 175 meV (lower). Experimental data are from Ref. 38

Fig. 9 Interface state envelope function at CdTe/HgTe interface.

Fig. 10 Band alignment in a GaAs/AlAs superlattice. The solid line denotes the Γ band edges, the dashed line the X band edge, and the dot-dashed line the L band edge.

Fig. 11 (a) Brillouin zone of the bulk fcc lattice. (b) Brillouin zone of an N/M superlattice with even $N + M$. (c) Brillouin zone of the superlattice when $N + M$ is odd.

Fig. 12 Energy levels at $\bar{\Gamma}$ as functions of N for the N/N superlattices. Labels $n\Gamma$ and nX denote the number of a level and its origin in bulk conduction valley. An open square denotes even parity and a cross odd parity.

Fig. 13 Band structure along $(a^*, 0, fc^*)$ for superlattices (a) 8/10, (b) 7/11, (c) 7/10, and (d) 8/11.

Fig. 14 Lowest two energy subbands along $(a^*, 0, q_z)$ for the rough interface. The subbands are calculated by allowing the first Ga plane to be mixed with different Al fractions. The solid lines are the subbands of zero Al fraction, $(GaAs)_8(AlAs)_{10}$, and the dotted, short-dash, long-dash, dot-short-dash lines denote the subbands of the Al fractions 0.2, 0.4, 0.6, 0.8, repectively. When Al fraction equals to 1, the superlattice becomes 7/11 (dot-long dash). (After Ref. 44.)

Fig. 15 Normal magnetic field turning valence subbands into sets of discrete Landau levels.

Fig. 16 Magnetic field parallel to the interface plane of a superlattice.

Fig. 17 The left panel shows the subbands at $B = 0$ and $k_x = 0, k_y = 0$. The solid line uses the renormalized mass m_b and the dashed line uses the bulk effective mass m_b^*. The right panel shows the first 15 levels at $B = 10T$ and $k_x = 0$.

Fig. 18 Transition energy between two lowest bands at $R_z = 0$ as a function of the magnetic field. Squares with error bars are the measured energies for parallel field and circles with error bars are for normal field. The solid line is calculation with the renormalized mass in the barrier and the dashed line is calculation with the bulk mass in the barrier.

Fig. 19 Diagrams for the conduction band polarization part with self-energy and vertex corrections due to impurity. The broken line represents interaction with impurity.

Fig. 20 Magnetic field dependence of the screening parameter q_s, electron self-energy terms, screened exchange $\Sigma_{ex}^*(0)$ and correlation hole $\Sigma_{ch}^*(0)$. The electron density is $1.0 \times 10^{11} cm^{-2}$

Fig. 21 Transition energy between conduction and valence band Landau levels in a InP/InGaAs quantum well. Solid curves - theory (Ref. 61); dots - experiment (Ref. 64).

Fig. 22 Three-step processes in luminescence.

Fig. 23 Luminescence in the back-scatter configuration.

Fig. 24 Circular polarization spectra for: (a) a p-doped quantum well, (b) an n-doped well, and (c) an undoped well. The excitation energy is measured relative to the $1h \rightarrow 1c$ transition threshold. Solid lines are calculation from Ref. 70 and dashed lines are experiment from Ref. 66.

Fig. 25 Luminescence in the wave-guide configuration.

Fig. 26 Calculated luminescence spectra for the polarizations normal and parallel to the interface plane due to simple recombination.

Fig. 27 Unstressed and stressed luminescence spectra: (a) experiment, (b) theory. (After Ref. 71.)

Fig. 28 Many-electron processes in luminescence. The line denotes the electron or hole propagator in the conduction subband, the broken line the hole in valence subband, and the wavy line the photon or screened Coulomb interaction. See text for explanation of the diagrams.

Fig. 29 Stress effects on the subband structure. (After Ref. 71.)

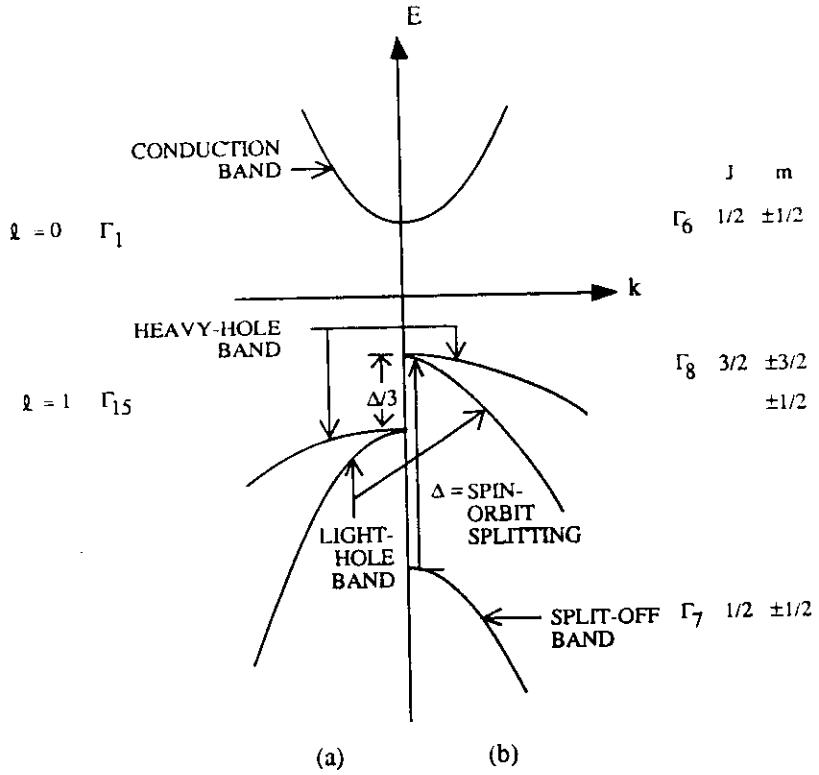

Figure 1

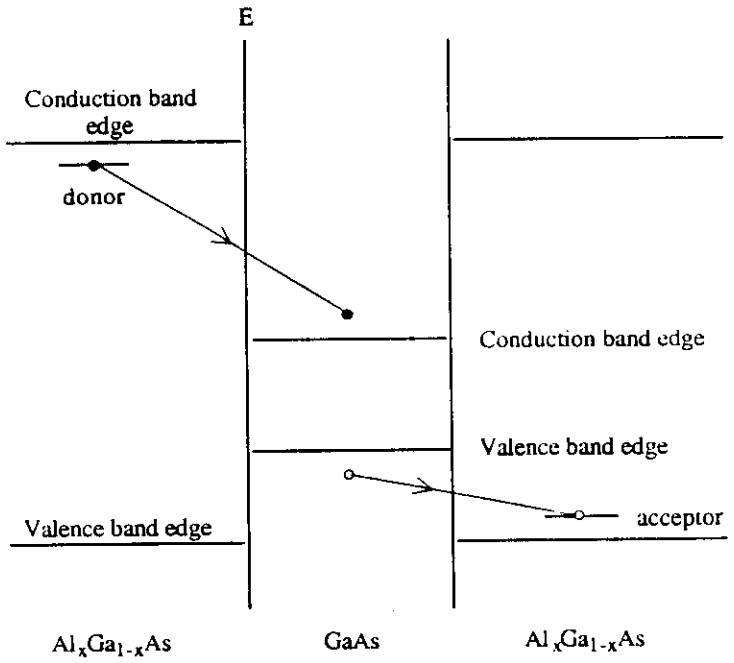

Figure 2

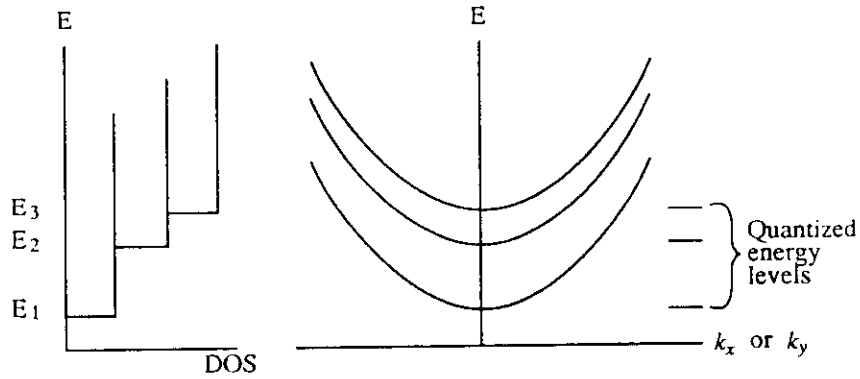

Figure 3

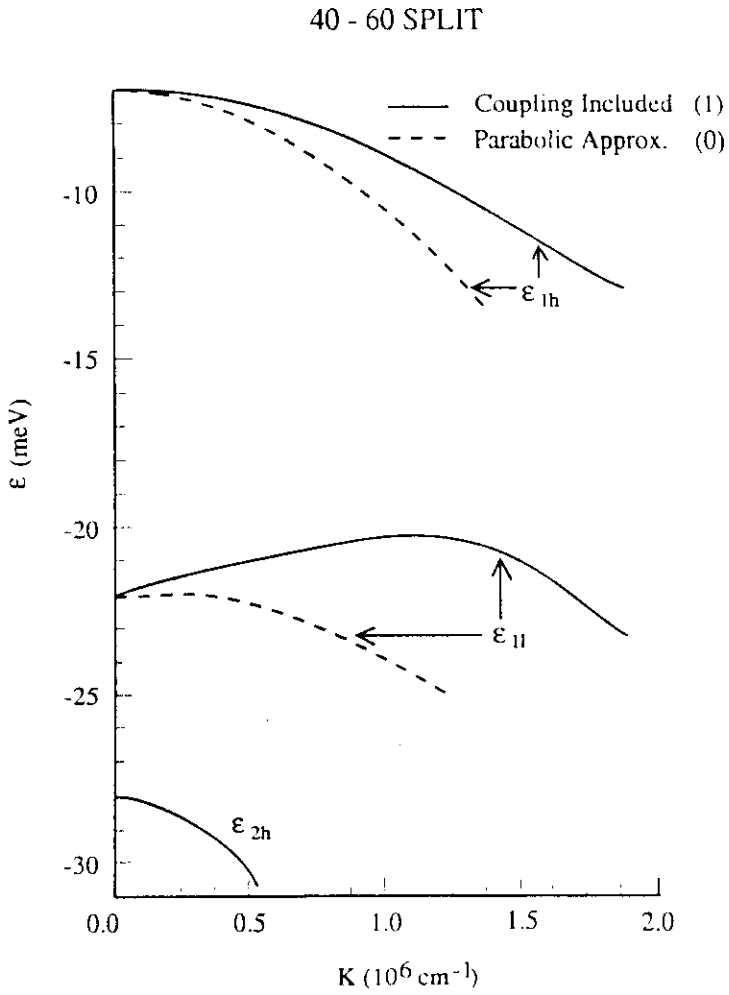

Figure 4

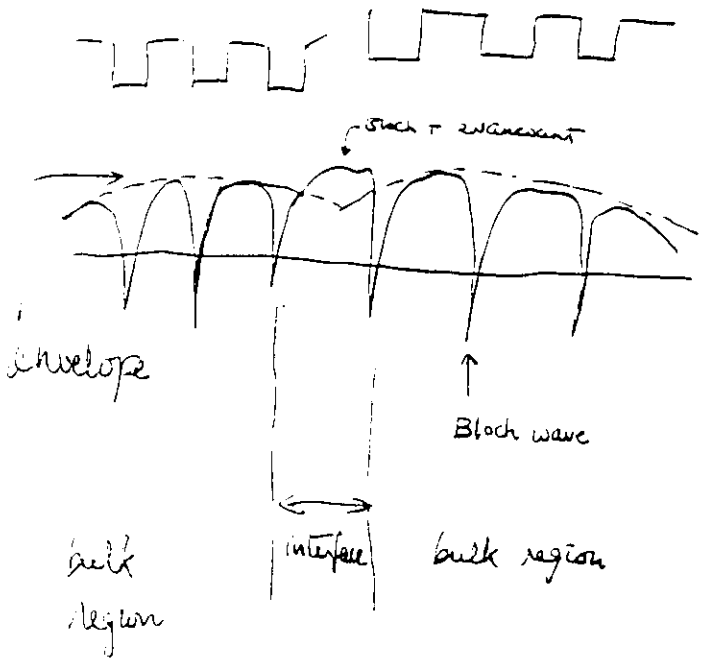

Figure 5

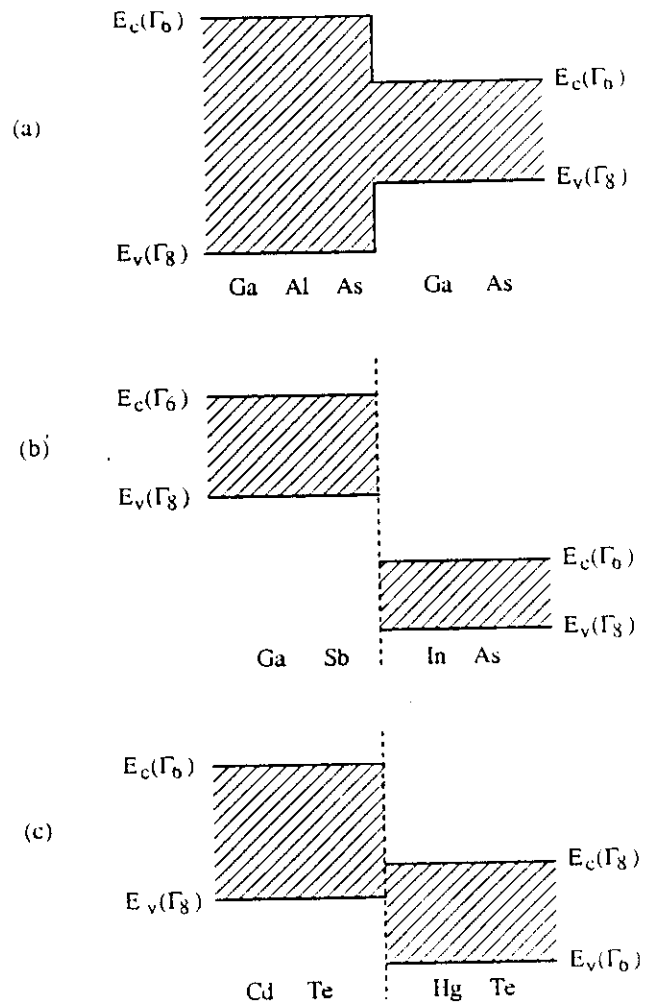

Figure 6

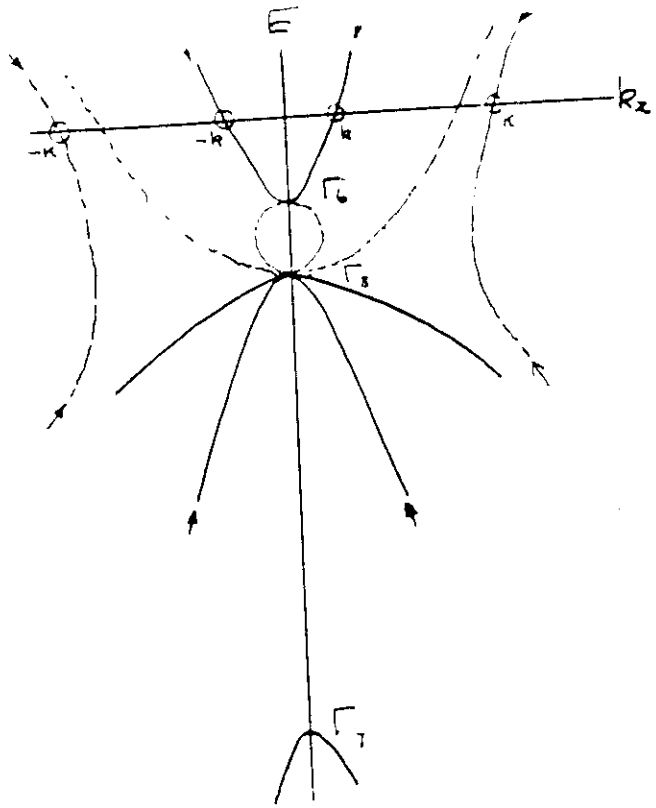

Figure 7

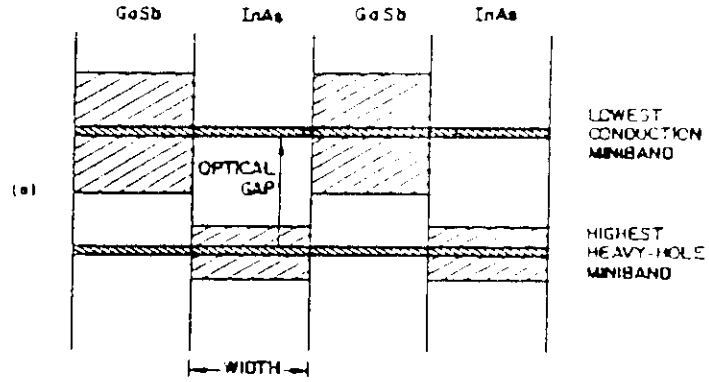

(a)

Figure 8a

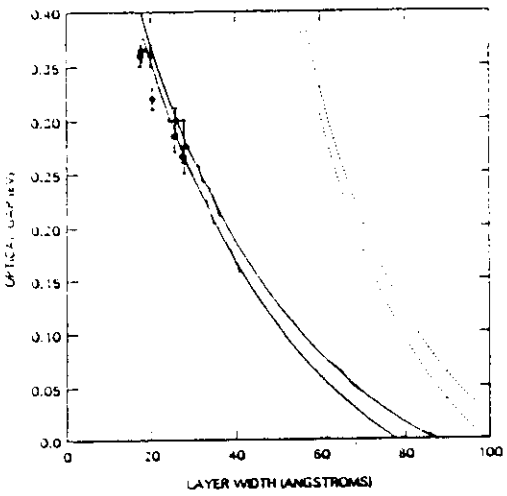

Figure 8b

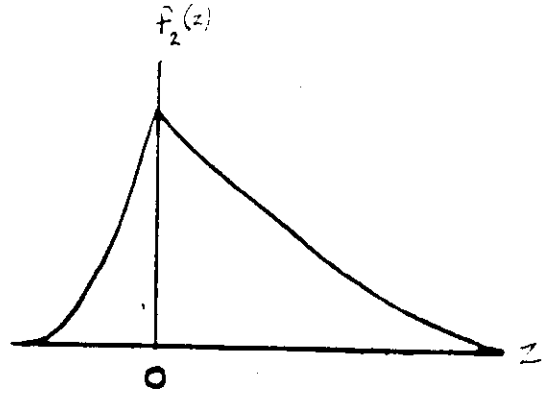

Figure 9

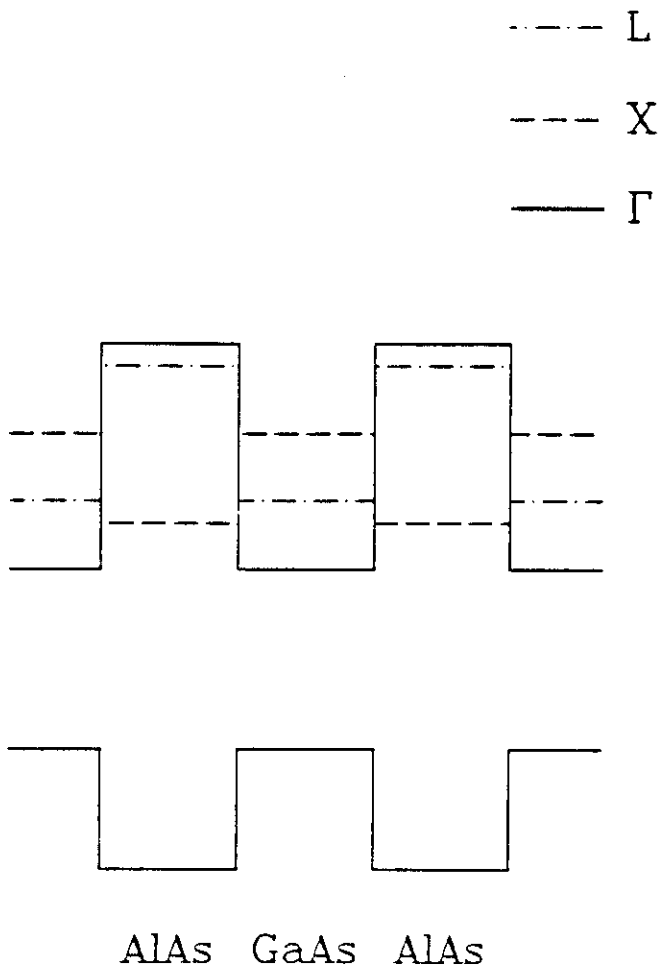

Figure 10

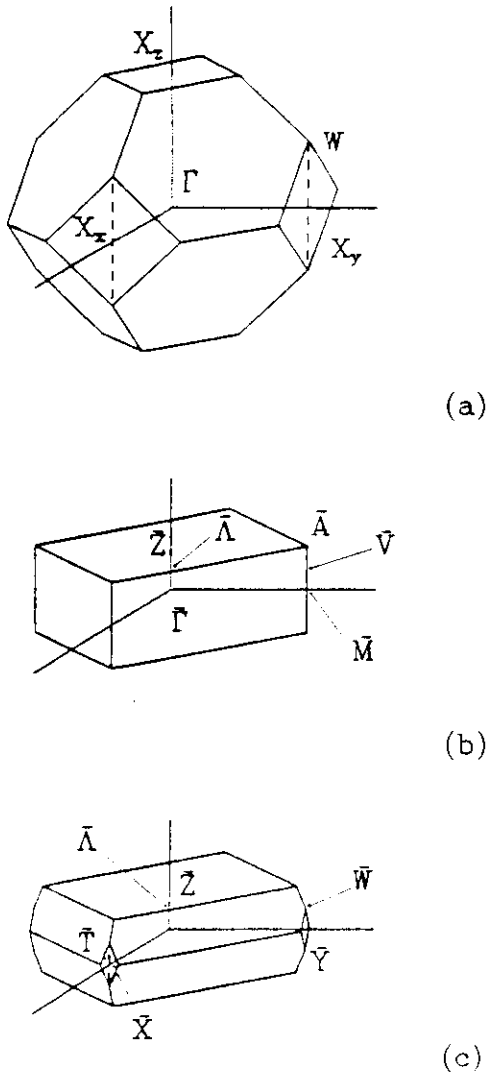

Figure 11

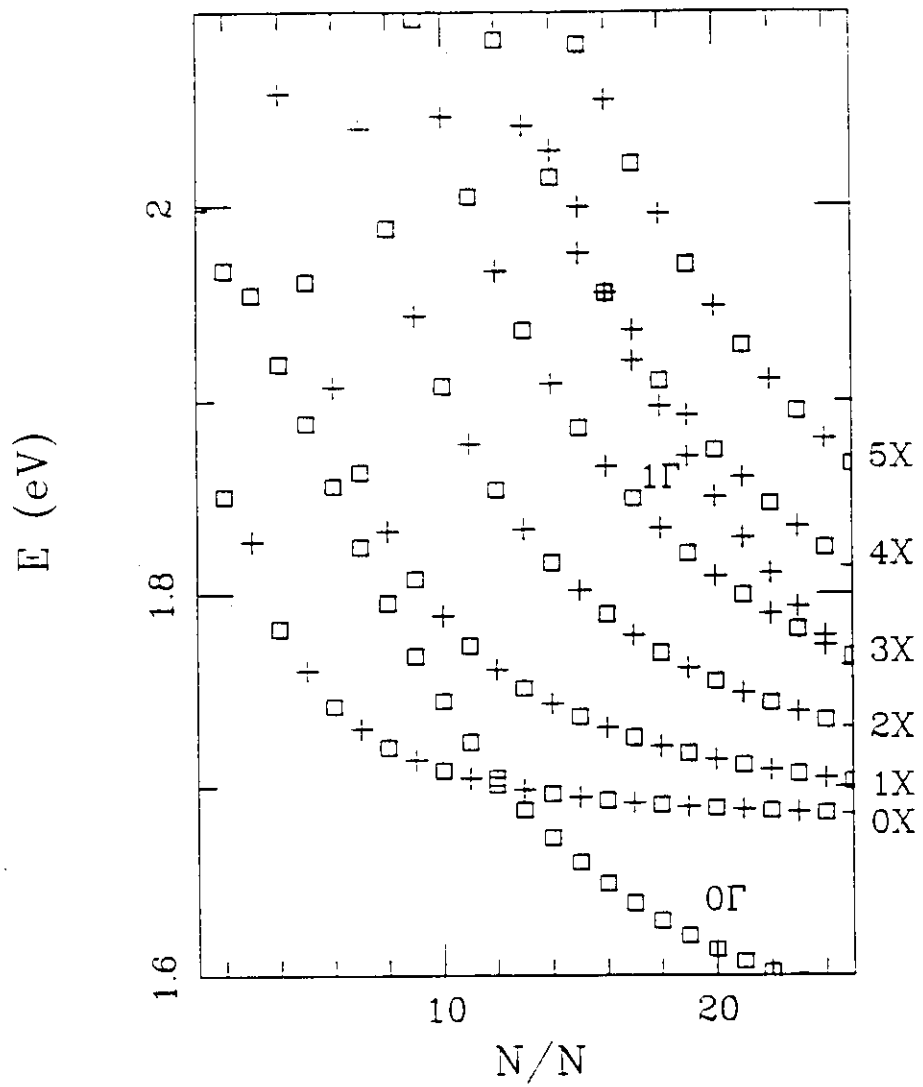

Figure 12

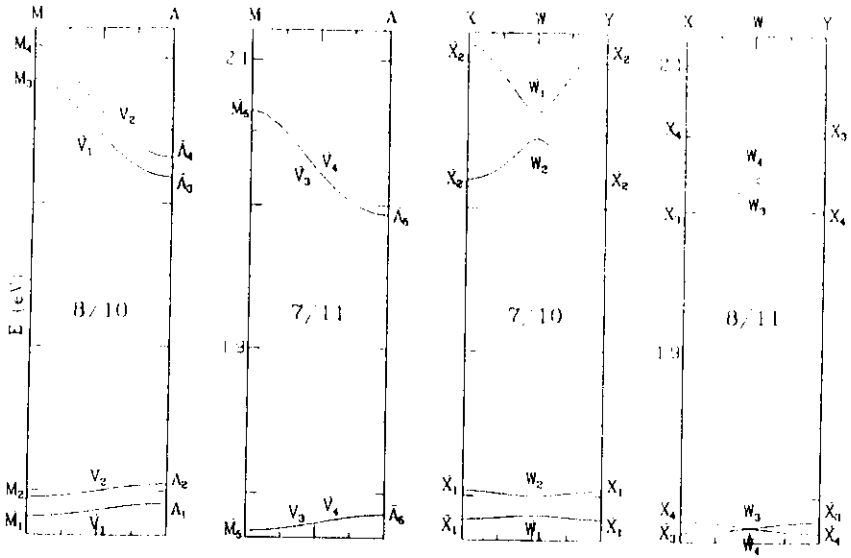

Figure 13

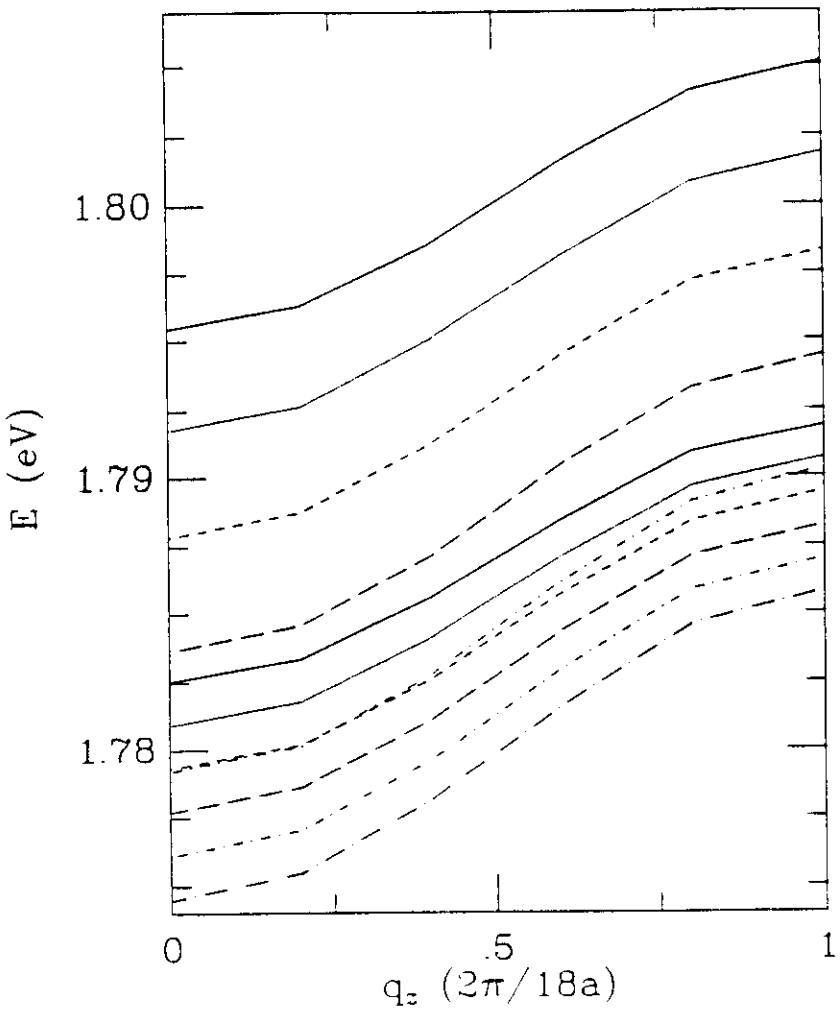

Figure 14

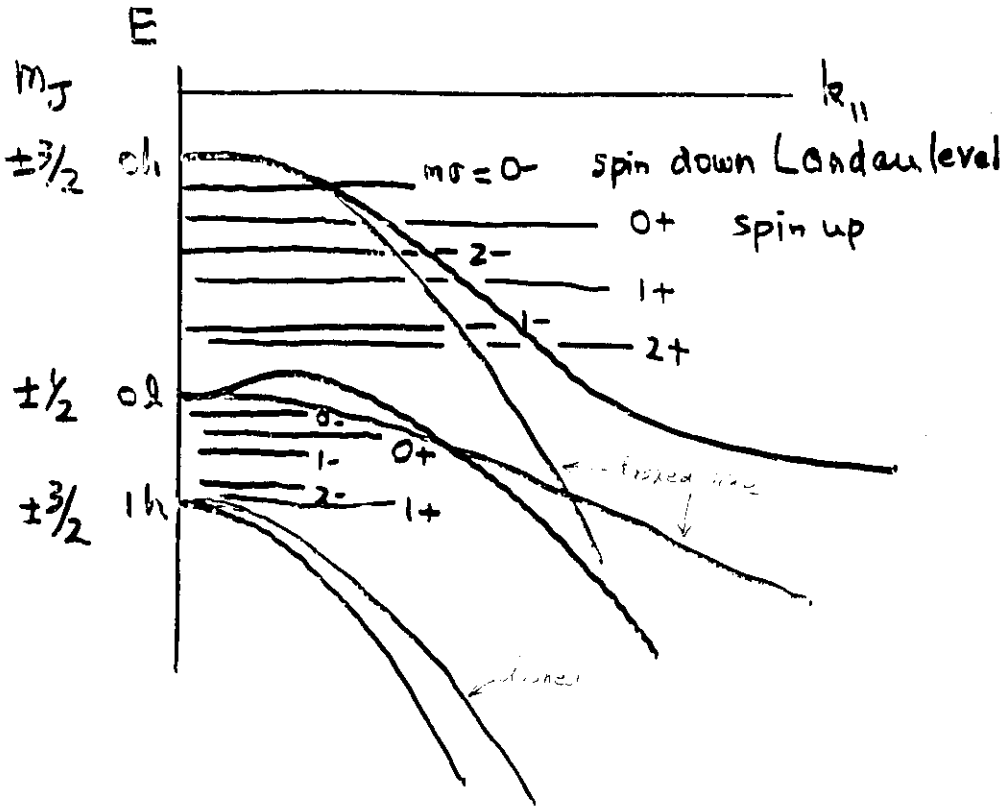

Figure 15

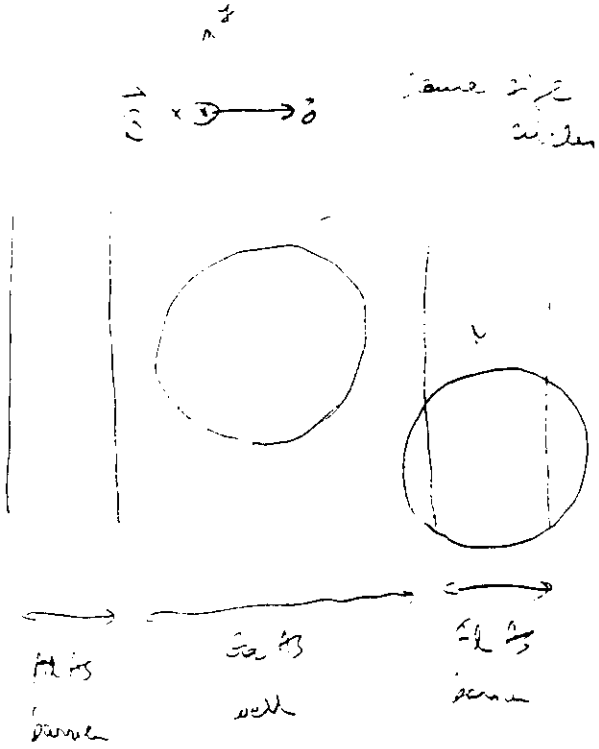

Figure 16

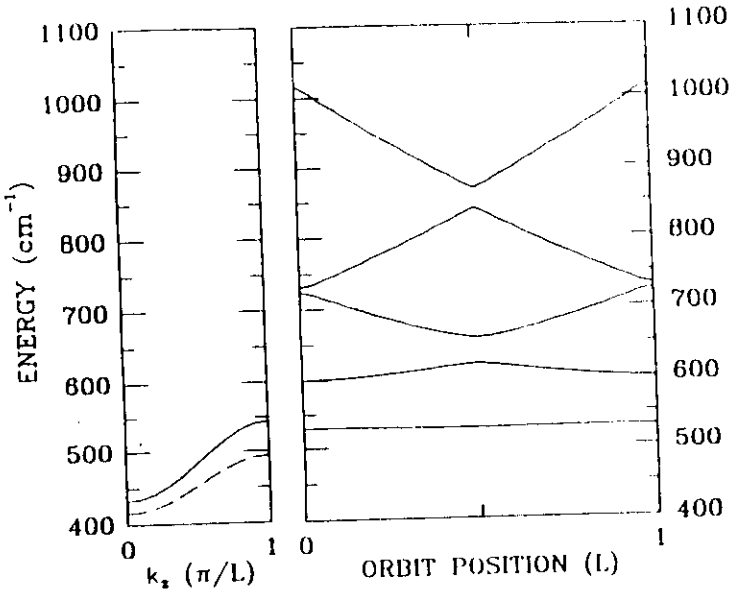

Figure 17

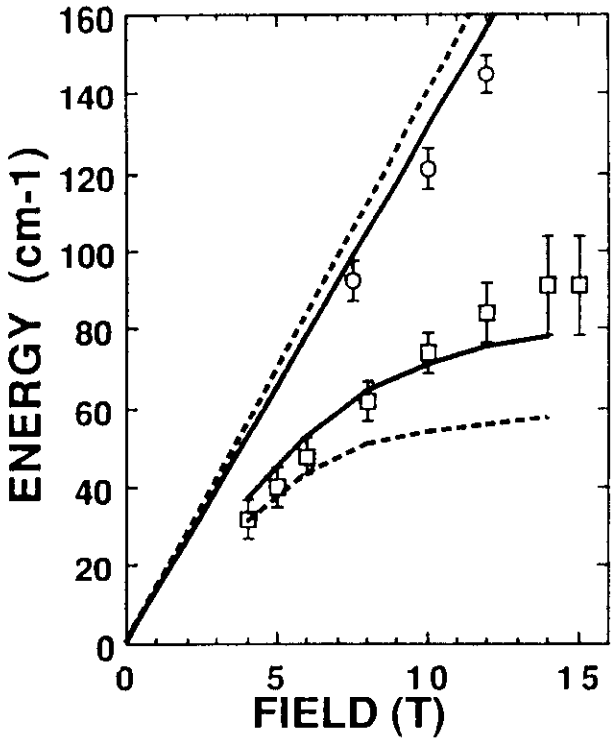

Figure 18

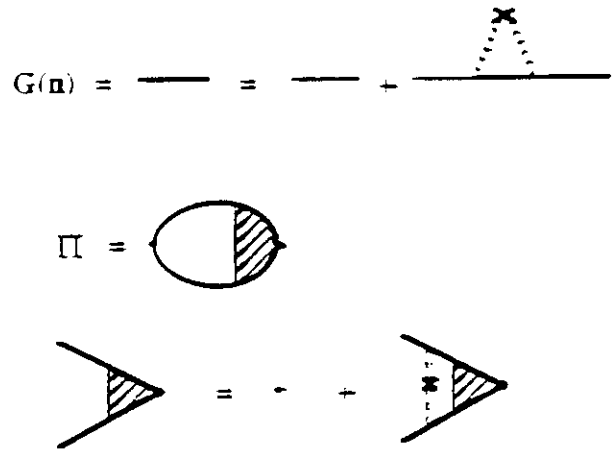

Figure 19

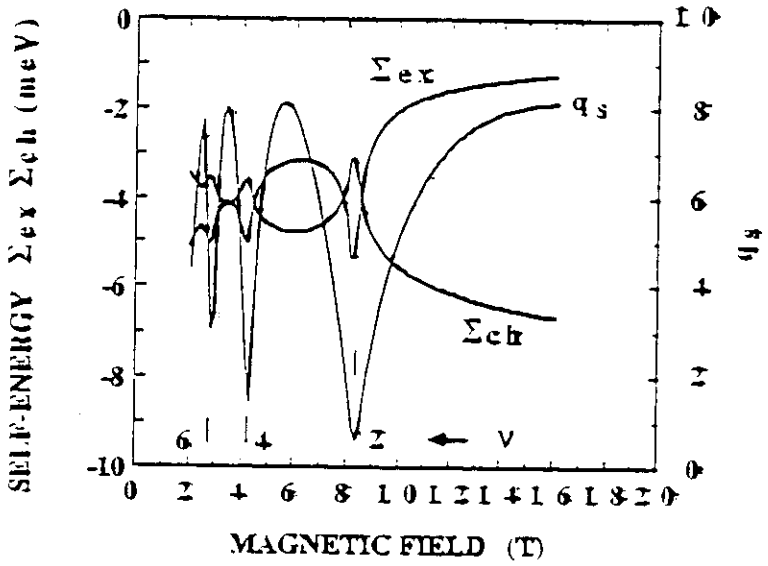

Figure 20

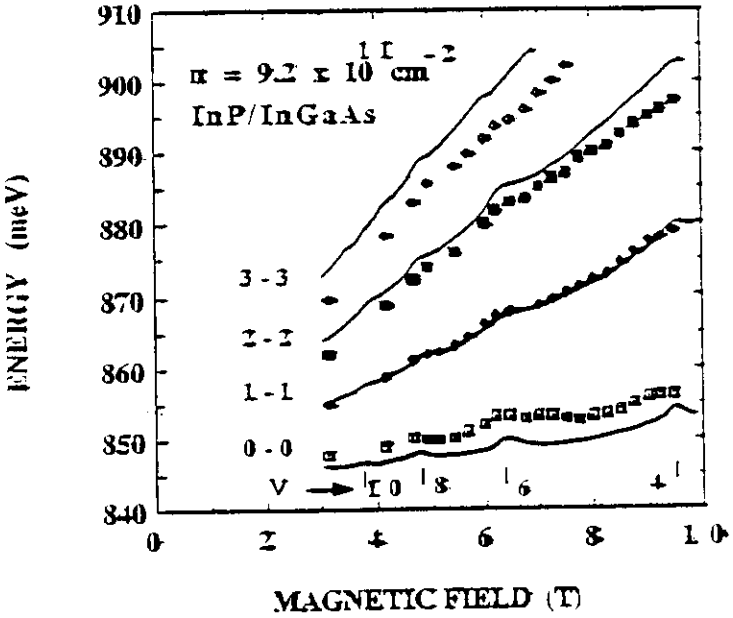

Figure 21

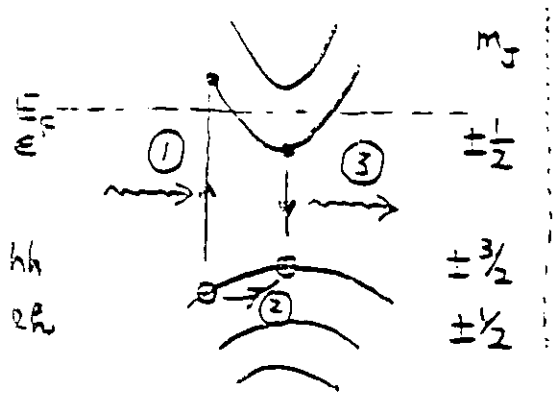

Selection rule

Δm_J

I_x ± 1

I_z 0

$m_{\frac{1}{2}} - m_{\frac{3}{2}} = m_{photon}$

Figure 22

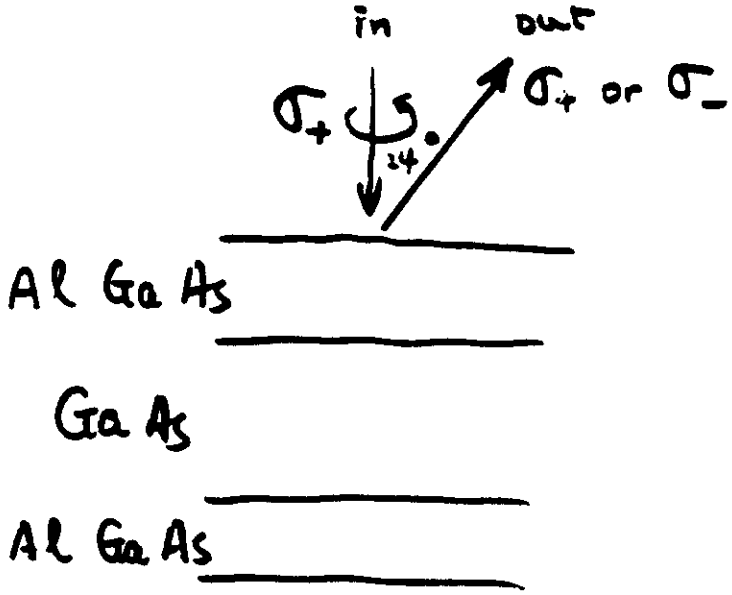

Figure 23

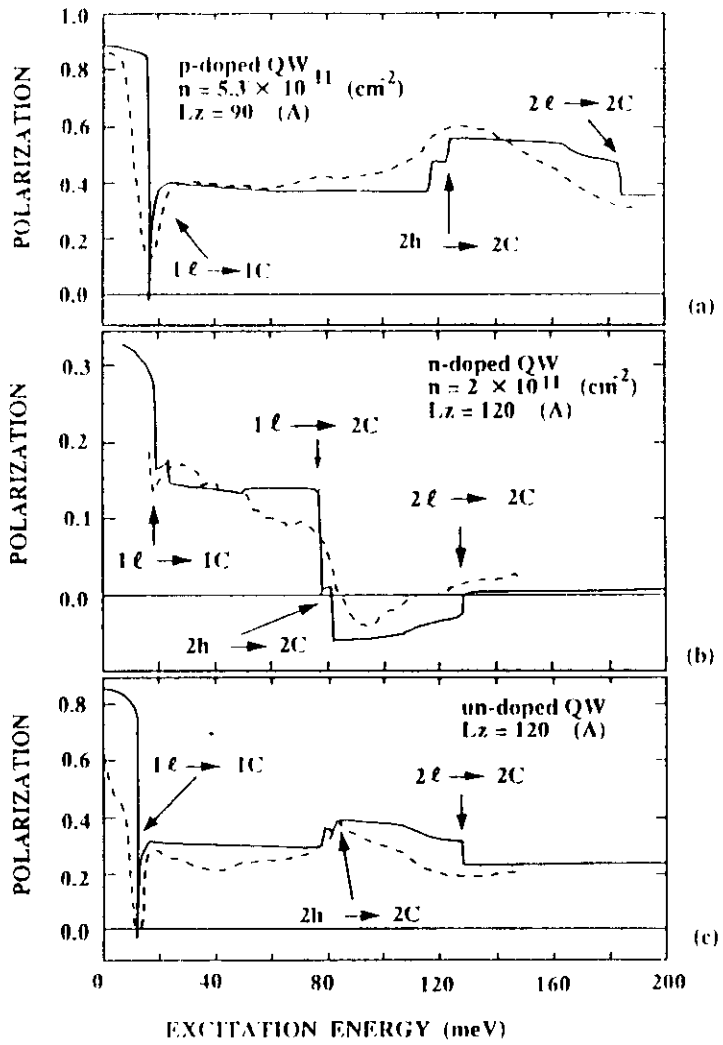

Figure 24

Fig. 25

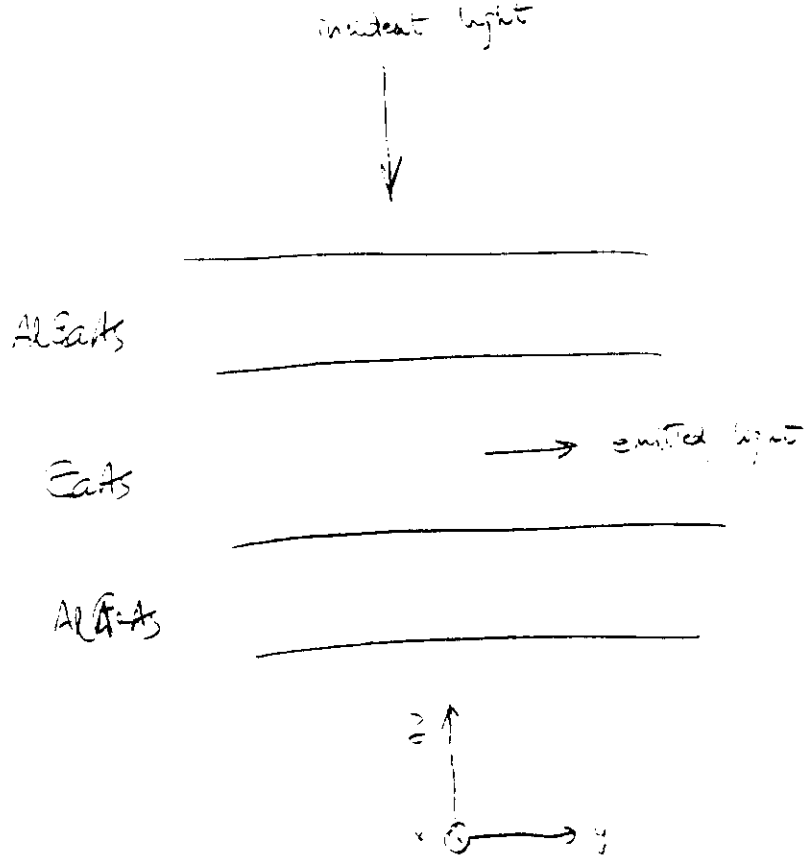

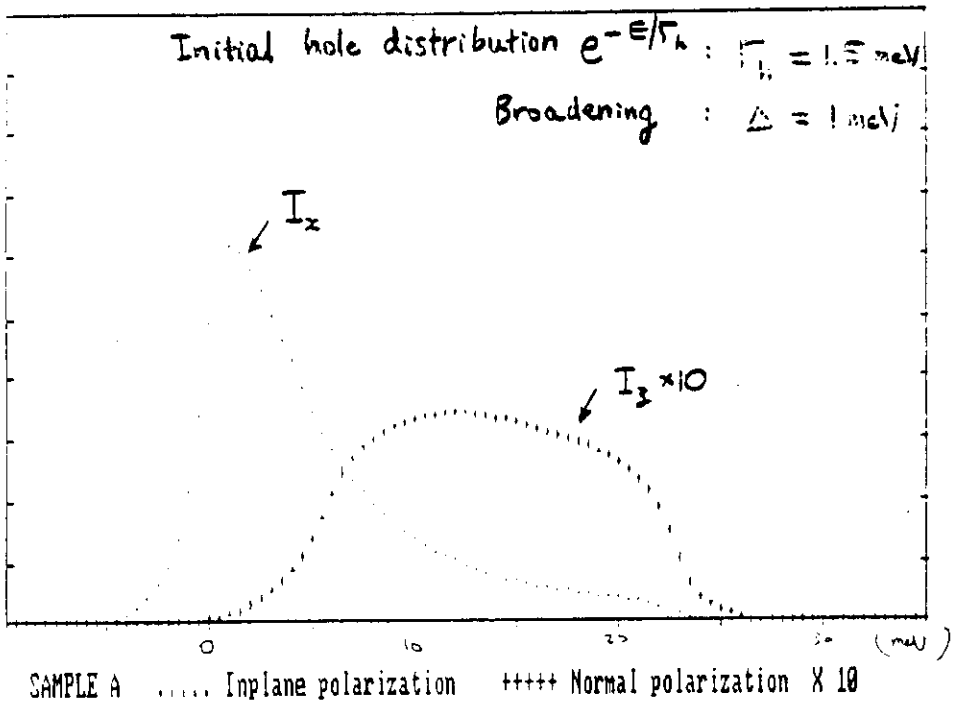

Figure 26

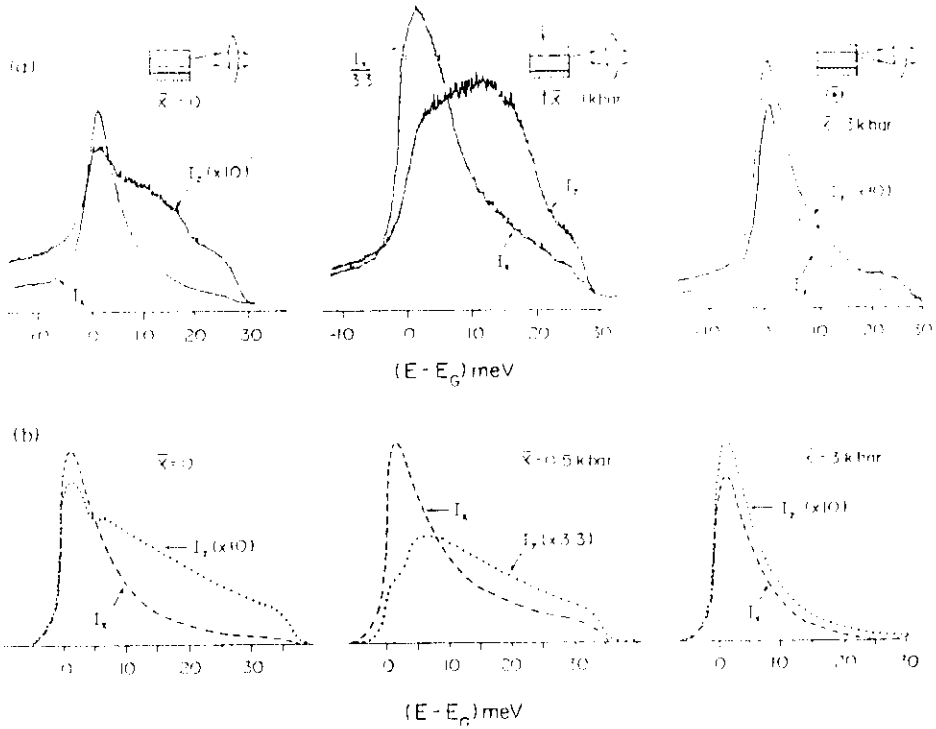

Figure 27

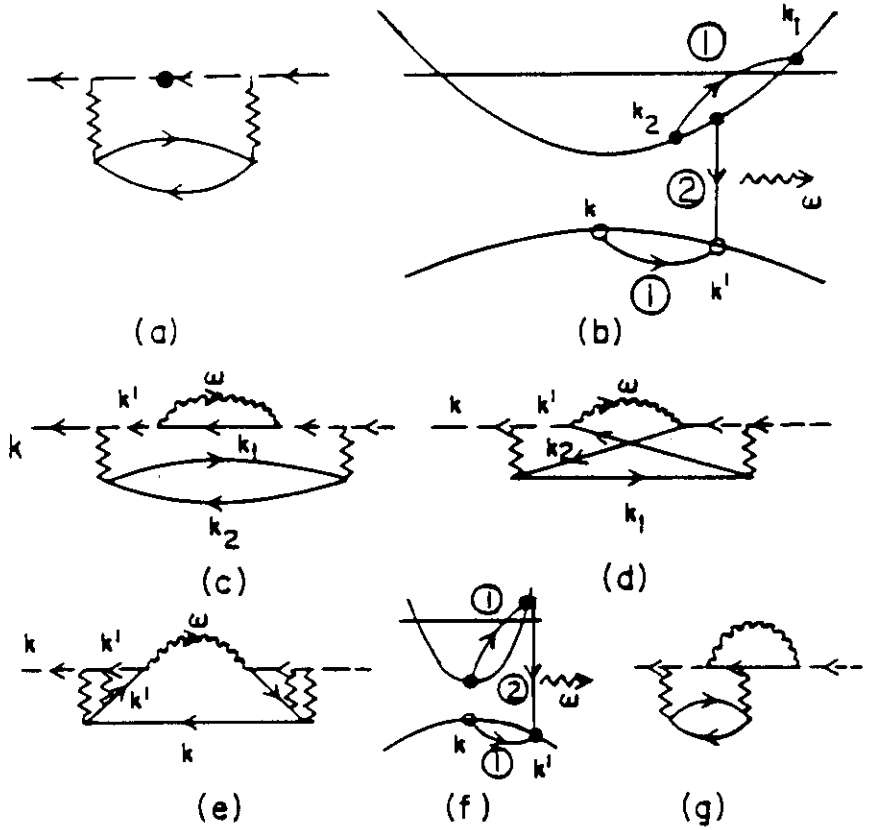

Figure 28

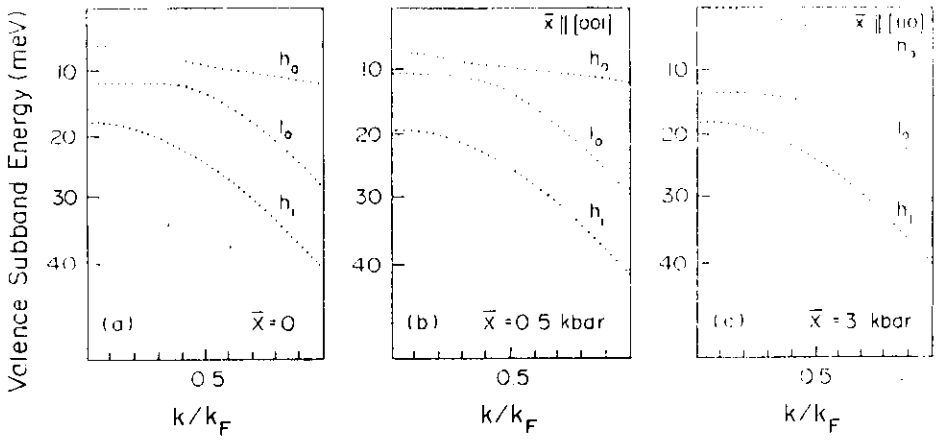

Figure 29